



## Plume Characterisation – Laboratory Studies

**Peter Fearn<sup>1,3</sup>, Passang Dorji<sup>1,3</sup>, Mark Broomhall<sup>1,3</sup>, Paul Branson<sup>2,3</sup>, Nick Mortimer<sup>2,3</sup>**

<sup>1</sup> *Department of Physics and Astronomy, Remote Sensing and Satellite Research Group, Science and Engineering, School of Science, Curtin University, Perth, Western Australia, Australia*

<sup>2</sup> *CSIRO Oceans and Atmosphere Flagship, Perth, Western Australia, Australia*

<sup>3</sup> *Western Australian Marine Science Institution, Perth, Western– Australia, Australia*

## WAMSI Dredging Science Node

Final report

Theme 3 | Project 3.2.2

December 2018





## WAMSI Dredging Science Node

The WAMSI Dredging Science Node is a strategic research initiative that evolved in response to uncertainties in the environmental impact assessment and management of large-scale dredging operations and coastal infrastructure developments. Its goal is to enhance capacity within government and the private sector to predict and manage the environmental impacts of dredging in Western Australia, delivered through a combination of reviews, field studies, laboratory experimentation, relationship testing and development of standardised protocols and guidance for impact prediction, monitoring and management.

### Ownership of Intellectual property rights

Unless otherwise noted, any intellectual property rights in this publication are owned by the Western Australian Marine Science Institution, the Australian Institute of Marine Science and the University of Western Australia.

### Copyright

© Western Australian Marine Science Institution

All rights reserved.

Unless otherwise noted, all material in this publication is provided under a Creative Commons Attribution 3.0 Australia Licence. (<http://creativecommons.org/licenses/by/3.0/au/deed.en>)



### Funding Sources

The \$20 million Dredging Science Node is delivering one of the largest single issue environmental research programs in Australia. This applied research is funded by **Woodside Energy, Chevron Australia, BHP Billiton and the WAMSI Partners** and designed to provide a significant and meaningful improvement in the certainty around the effects, and management, of dredging operations in Western Australia. Although focussed on port and coastal development in Western Australia, the outputs will also be broadly applicable across Australia and globally.

This remarkable **collaboration between industry, government and research** extends beyond the classical funder-provider model. End-users of science in regulator and conservation agencies, and consultant and industry groups are actively involved in the governance of the node, to ensure ongoing focus on applicable science and converting the outputs into fit-for-purpose and usable products. The governance structure includes clear delineation between end-user focussed scoping and the arms-length research activity to ensure it is independent, unbiased and defensible.

And critically, the trusted across-sector collaboration developed through the WAMSI model has allowed the sharing of hundreds of millions of dollars worth of environmental monitoring data, much of it collected by environmental consultants on behalf of industry. By providing access to this usually **confidential data**, the **Industry Partners** are substantially enhancing WAMSI researchers' ability to determine the real-world impacts of dredging projects, and how they can best be managed. Rio Tinto's voluntary data contribution is particularly noteworthy, as it is not one of the funding contributors to the Node.

### Funding and critical data

### Critical data



## Legal Notice

The Western Australian Marine Science Institution advises that the information contained in this publication comprises general statements based on scientific research. The reader is advised and needs to be aware that such information may be incomplete or unable to be used in any specific situation. This information should therefore not solely be relied on when making commercial or other decision. WAMSI and its partner organisations take no responsibility for the outcome of decisions based on information contained in this, or related, publications.

**Year of publication:** 2018

**Metadata:** <http://catalogue.aodn.org.au/geonetwork/srv/en/metadata.show?uuid=4d961aed-906c-4777-927d-60fc243a318e>

**Citation:** Fearn P, Dorji P, Broomhal M, Branson P, Mortimer N, (2018). Plume Characterisation–Laboratory Studies. Report of Theme 3 – Project 3.2.2, prepared for Dredging Science Node, Western Australian Marine Science Institution, Perth, Western Australia, 57pp.

**Author Contributions:** Wrote the report PF, PD, MB, PB, NM

**Corresponding author and Institution:** Peter Fearn (Curtin University).

**Competing Interests:** The commercial investors had no role in the data analysis, data interpretation, the decision to publish or in the preparation of the manuscript. The authors have declared that no competing interests exists.

**Acknowledgments:** National Computational Infrastructure.

**Collection permits/ethics approval:** No collection occurred in the production of this report.

## Front cover images (L-R)

Image 1: Trailer Suction Hopper Dredge *Gateway* in operation during the Fremantle Port Inner Harbour and Channel Deepening Project. (Source: OEPA)

Image 2: Top down view of instruments and agitator in the test tank after measurements had been taken at increasing sediment concentrations and then the tank drained.

Image 3: Dredge plume at Barrow Island. Image produced with data from the Japan Aerospace Exploration Agency (JAXA) Advanced Land Observing Satellite (ALOS) taken on 29 August 2010.

Image 4: TSS concentration image derived from Landsat-8 data. Images by Mark Broomhall

# Contents

- EXECUTIVE SUMMARY ..... I**
- RESIDUAL KNOWLEDGE GAPS ..... II**
- GLOSSARY OF TERMS ..... III**
- 1 INTRODUCTION ..... 1**
- 2 MATERIALS AND METHODS ..... 1**
  - 2.1 SEDIMENT SAMPLES .....1
  - 2.2 EXPERIMENT DESIGN AND DATA PROCESSING .....4
    - 2.2.1 *Experiment Design*.....4
    - 2.2.2 *Experiment Procedure* .....5
  - 2.3 INSTRUMENTAL AND DATA PROCESSING.....5
    - 2.3.1 *SBE 19 plus SeaCAT*.....5
    - 2.3.2 *WetLabs ac-s* .....6
    - 2.3.3 *HobiLabs Hydroscat-6*.....7
    - 2.3.4 *AQUAscat 1000R* .....7
    - 2.3.5 *LISST-ABS* .....7
    - 2.3.6 *Sequoia Scientific LISST 100X and data processing procedure* .....8
  - 2.4 DATA MERGING .....8
- 3 RESULTS ..... 8**
  - 3.1 TSS MEASUREMENT .....8
  - 3.2 AC-S AND HYDROSCAT-6 MEASUREMENTS .....9
    - 3.2.1 *Absorption and Scattering Coefficient*.....9
    - 3.2.2 *Backscattering coefficient* .....11
    - 3.2.3 *Mass-specific backscattering coefficient*.....13
    - 3.2.4 *The Backscattering probability*.....13
    - 3.2.5 *Backscattering spectral slope* .....14
  - 3.3 LISST MEASUREMENTS .....15
  - 3.4 WETLABS TURBIDITY METER .....17
  - 3.5 ACOUSTIC SENSORS .....20
  - 3.6 INTERCOMPARISON OF INSTRUMENT RESULTS .....22
    - 3.6.1 *Particle size distribution (PSD) parameters and particulate backscattering coefficients* .....22
    - 3.6.2 *NTU and LISST*.....25
- 4 DISCUSSION AND CONCLUSIONS ..... 27**
  - 4.1 TSS, NTU AND SCATTERING .....27
  - 4.2 PARTICLE SIZE DISTRIBUTIONS .....28
  - 4.3 PARTICLE DENSITIES .....31
- 5 REFERENCES ..... 32**
- 6 APPENDICES ..... 33**
  - APPENDIX A. TSS VALUES FOR WATER/SEDIMENT SAMPLES .....33
  - APPENDIX B. NTU TIME SERIES .....38
  - APPENDIX C. TSS VS OBS NTU REGRESSIONS. ....40
  - APPENDIX D. TSS VS WETLABS NTU REGRESSIONS .....42
  - APPENDIX E. TSS VS LISST TOTAL VOLUME CONCENTRATION REGRESSIONS.....45



## Executive Summary

Water quality associated with dredge operations is often monitored and reported in terms of Nephelometric Turbidity Units (NTU), a specific measure of the light scattered by particulate matter suspended in the water column. This water quality measurement provides information on water clarity but provides little data on the particle size and dynamics or the optical properties of the sediment. From the perspective of understanding light fields within the water column, or light reflected from the ocean that might be detected by remote sensing instruments, it is the specific optical properties of spectral scattering and absorption that are important. There exists a range of optical sensors that measure optical characteristics intimately related to turbidity so it is of interest to understand the relationships between traditional NTU measurements and these other optical measures of water clarity.

Measurements of total suspended solids (TSS) are often reported within a suite of water quality measurements. The TSS is a good indicator of turbidity, but also is related to the total mass of particulates suspended in a column of water and in turn the potential settlement of particulates on the benthos. The remote sensing product most commonly reported for turbid coastal waters dominated by inorganic particulates is TSS.

Optical measurements more complex than the simple NTU procedure can be employed to determine particle size distribution (PSD). Knowledge, or reasonable assumptions, of the PSD is critical for estimating the proportions of particles that will settle out of a water column and those that will be transported some distance from the source of particulates.

Notwithstanding the potential of remote sensing for monitoring water quality associated with dredge operations (see Project 3.2.1), collection of samples for input to models, and characterisation of optical properties and PSD of a water mass is typically carried out using in situ methods, thus is costly and labour intensive. We collected sediment samples from the seabed associated with dredge operations in waters adjacent to Onslow, WA, and subjected these samples to a series of controlled tank-based studies to measure optical and physical parameters of interest, including NTU, scattering and backscattering coefficients, PSD and acoustic scattering. The results showed, as was expected, very high correlation between the various scattering measurements, but also highlighted some of the differences.

In particular, we observed a non-linearity between the NTU and TSS which was more obvious over the large range of TSS measured. It is clear that **calibration of an NTU sensor needs to be based on the full range of TSS concentrations expected to be encountered in the field, and the number of calibration points must be sufficient to characterise the potential non-linearity.**

We also demonstrated a significant range of TSS/NTU calibration ratios of the sediment samples collected from close proximity to the dredge operations and measured in the tank (ranging from 2.2 to 2.8), in contrast to field-based calibrations of 1.1. **These results do not support the idea to collect sediment samples in the field to undertake TSS/NTU calibrations by resuspension.** The extent and duration of the field program was not sufficient to fully explore the potential variability of the TSS/NTU calibration, but it would be sensible for those undertaking TSS monitoring using NTU sensors (or similar scattering sensors) to periodically collect concurrent water samples for gravimetric determination of TSS to monitor the TSS/NTU calibration.

Also, the majority of re-suspended sediment samples measured using a LISST instrument were characterised by a bi-modal PSD, in contrast to field-based measurements of the PSD that typically were not bi-modal. However, field samples derived from core samples and measured in-lab with a Malvern Analytical Mastersizer 2000 did often display a bi-modal PSD. We surmise that either samples collected from the substrate, either by core or grab or other collection method may naturally display a bi-modal distribution representative of a fine layer of clay and fine silt from dredging having settled on an otherwise coarse sandy seabed, or, the act of sample collection and re-suspension significantly changes the PSD from the naturally occurring, possibly due to effects of flocculation. Therefore, we suggest it is **unwise to attempt to use this collection and re-suspension process to obtain accurate estimates of in-field PSD properties.**

### Considerations for predicting and managing the impacts of dredging

Turbidity is commonly reported in units of NTU. It is important to understand that an NTU sensor is simply a specific type of light scattering sensor, with the calibration referenced to a specific concentration of formazin in water. The amount of light scattered by natural particulates depends on factors such as particle shape, size (or PSD), colour and angle of light scattering. As a consequence, the relationship between NTU measured in natural waters is not expected to be exactly correlated with TSS. Sometimes an NTU sensor, or the NTU readings obtained, may be calibrated to TSS, but if the physical/optical properties of the particulates vary from the calibration samples, the NTU versus TSS relationship will break down.

A number of scattering sensors were tested and shown to all produce highly correlated, but different results. Essentially any (reasonable) scattering sensor could be used to collect data that may be correlated with TSS. Some scattering sensors are designed to provide meaningful optical scattering properties. These sensors could be used to estimate TSS load, as well as provide optical data for input to radiative transfer models, which in turn could be used to develop and validate remote sensing algorithms, or spectral light intensity in the water column and at the substrate. For all in situ sensors, users need to be careful to understand the nuances of the differences and similarities.

Sediment samples collected from the substrate and then re-suspended in a laboratory setting cannot be used to infer the optical or PSD characteristics of the naturally occurring suspended sediment in the ocean. The NTU to TSS calibration should be carried out in the field during the monitoring program, with the calibration being tracked through time by comparison with water samples collected and subjected to gravimetric analysis.

The same recommendation holds for the determination of suspended sediment PSD. **Substrate samples cannot be collected and re-suspended with the intent of determining water column PSD.** The samples analysed by resuspension in this work displayed significantly different PSDs to those measured in situ during the field program.

### Residual Knowledge Gaps

The relationships between TSS and optical/acoustic scattering measurements, including NTU, are quite robust and usually accepted as reasonably linear, at least over a moderate TSS range. However, the specific relationships are typically derived using empirical methods. We have demonstrated empirically derived relationships and shown the variability in ‘calibration’ across a range of sediment samples. A degree of the variability in calibration is attributed to the characteristics of the particle size distribution, with moderate relationships shown for TSS to NTU ratios and PSD metrics. The majority of sediment samples were collected in the Onslow region, with only two collected from further afield, thus the results (calibration parameters) presented should not be applied to sediments in other regions. In fact, the Onslow sediment samples were collected during only three field campaigns, thus may not be representative of the wide range of sediment characteristics that might be expected during all stages of a dredge campaign. The two non-Onslow sediment samples highlighted the potential degree of variability. Further, comparison of the TSS/NTU calibration to that carried out in situ during the field program highlighted significant differences. This work demonstrated the impact of PSD on the calibration of TSS/NTU scattering sensors, but cannot be considered definitive and encompassing of all situations in any way. A more extensive investigation using in situ TSS, scattering and PSD data representative of a wide range of sediment types, preferably sourced from various locations during different stages of dredging, would increase the understanding of the complex TSS to scattering relationships. An improved understanding would potentially lead to more robust calibration protocols, and possibly improved quality of data used as input to hydrodynamic models.

We have demonstrated some of the difficulties in undertaking seemingly simple optical measurements in the complex optical environment of turbid water. We were able to demonstrate relationships or interdependencies between various measured and derived parameters, but we must stress that many, if not all, of the optical measurements are affected by the PSD. In turn, the PSD is affected by the shear of the water column. We only

undertook measurements under one mode of mixing in the tank. The natural environment not only experiences mixing due to many different forces, but the energy regime varies considerably, from extremes of “glassed out” waters to cyclonic storms.

## Glossary of terms

ABS:	Acoustic Backscatter Sediment sensor
AIMS:	Australian Institute of Marine Science
aw:	pure water absorption TSS
bb:	scattering coefficient
bbp* ( $\lambda$ ):	mass-specific backscattering coefficient
bbp:	particulate backscattering coefficient
Bw:	scattering
CSIRO:	Commonwealth Scientific and Industrial Research Organization
CTD:	Conductivity Temperature Depth instrument
DPaW:	Department of Parks and Wildlife
LISST:	Laser <i>In Situ</i> Scattering and Transmissometry
NIR:	near infrared
NTU:	nephelometric turbidity unit
OBS:	Optical Backscattering Sensors
PS:	Particle Size
PSD:	Particle Size Distributions
S:	salinity
T:	temperature
TSS:	Total Suspended Sediment
TVC:	Total volume concentration



## 1 Introduction

Water quality monitoring is a routine operation during dredging to ensure compliance with limits established through the approval process, to ensure impacts are minimised during project implementation and to inform the adaptive management process with respect to the need for the development and implementation of appropriate intervention (EPA 2016). There are many parameters associated with water quality, but commonly water quality in coastal waters is associated with turbidity and volumetric measurement of water constituents (inorganic sediments, phytoplankton, detritus), in particular the total suspended sediment concentration (TSS). The turbidity and TSS concentration in coastal waters can be monitored using either space-borne remote sensing or traditional in situ techniques using a wide range of optical and acoustic instruments or water sampling methods (Evans et al., 2012; Islam et al., 2007).

Water column turbidity can be measured in situ using a variety of different optical sensors with each using a slightly different underlying principle and producing typically different units. Some instruments can measure turbidity based on light transmittance or attenuation and some instruments can estimate turbidity using acoustic scattering (Fearn et al. 2017a). However, most sensors designed specifically to measure turbidity typically rely on measurements of the scattering of light to derive a measure of water turbidity, reported as a mass-specific NTU (nephelometric turbidity unit). Some sensors that measure scattering of light can also provide an indication of particle size, or distribution of particle sizes, based on the relative differences in the scattering of light at different wavelengths or angles. In situ TSS measurements are often used to calibrate NTU sensors to derive estimates of TSS, however the optical scattering strength (NTU) varies for different particulate types due to differences in shape, refractive index and particle size distribution (PSD), therefore the calibration of the NTU sensor tends to be considered site-specific, or water mass-specific.

The range of optical sensors available in the market range in price from a few thousand to tens of thousands of dollars. Examples include Environmental Characterization Optics (ECO) series sensors, Optical Backscattering Sensors (OBS), HydroScat Optical Backscattering sensors, In situ Spectrophotometers (acs) and Laser *In Situ* Scattering and Transmissometry (LISST) instruments (Fearn et al. 2017a). In this study we performed comparative measurements using various common turbidity sensors, including optical scattering and acoustic scattering instrumentation, and compared and contrasted the results with respect to estimating particle load (TSS concentration), and/or Particle Size Distributions (PSDs). Studies were conducted in a controlled laboratory-based setting with a range of different sediment types primarily obtained from the Pilbara coast.

More specifically we:

- determined the particle size (PS) of sediment samples from Pilbara coastal waters using a sequoia scientific LISST 100X submersible particle size analyser and related PS to the particulate backscattering slope ( $\gamma_{bp}$  parameter) of HoboLabs HydroScat-6 data;
- compared PSD measurements in-tank to those collected in-field;
- established the relationship between turbidity and TSS concentration using the optical properties of particulate backscattering coefficient ( $b_{bp}$ ), scattering coefficient ( $b_b$ ) from HydroScat-6, Wetlabs ECO NTU and Campbell Scientific OBS3+ data.
- compared TSS/NTU calibrations conducted in-tank to those derived from in-field data.

## 2 Materials and Methods

### 2.1 Sediment Samples

The majority of sediment samples used in this experiment were obtained from the waters along the Pilbara coast near Onslow in northern Western Australia (see Figures 1–3 and Table 1. Details of the samples used in the experiments.). A small number of samples from other locations were used during initial testing of the equipment, and to provide contrast to the samples collected in the Onslow region.

Table 1. Details of the samples used in the experiments.

ID	Location Name	Latitude	Longitude	Experiment Date
S01	Kelmscott hills clay	-32.1302	116.0357	14/09/2015 02:45:00 PM
S02	Kelmscott hills clay	-32.1302	116.0357	08/12/2015 10:40:00 AM
S03	AIMS Sponge Site 1	-21.6020	115.092	09/12/2015 02:25:00 PM
S04	AIMS Sponge Site 2	-21.5155	115.033	10/12/2015 12:00:00 PM
S05	Direction Island NE	-21.5311	115.135	10/12/2015 03:38:00 PM
S06	DPaW Sites	-21.518	115.203	11/12/2015 11:30:00 AM
S07	J16 (CSIRO)	-21.588	115.088	11/12/2015 03:28:00 PM
S08	Locker Island	-21.717	114.926	14/12/2015 12:06:00 PM
S09	Ashburton Island NE	-21.588	114.939	14/12/2015 02:25:00 PM
S10	Riverton Bridge (Perth)	-32.017	115.900	15/12/2015 11:04:00 AM
S11	Credo (inland South WA)	-30.192	120.653	15/12/2015 02:36:00 PM
S12	D23 (CSIRO) Ashburton river mouth	-21.670	115.033	16/12/2015 10:52:00 AM
S13	D28 (CSIRO) dredge zone	-21.613	115.041	16/12/2015 02:24:00 PM
S14	J17 (CSIRO) 2km from shore	-21.618	115.103	08/11/2016 12:46:00 PM
S15	J19 (CSIRO) 2km from dredge zone	-21.619	115.076	09/11/2016 08:40:00 AM
S16	D26 (CSIRO) dredge zone	-21.631	115.036	09/11/2016 11:32:00 AM
S17	J8 (CSIRO) 2 km from dredge zone	-21.612	115.087	09/11/2016 02:38:00 PM
S18	J16 (CSIRO) 3 km from dredge zone	-21.588	115.088	10/11/2016 11:02:00 AM

The waters in Onslow have been impacted by dredging activities for the Wheatstone project (Wheatstone Project; see Ministerial Approval Statement MS873, available on the WA EPA website: <http://www.epa.wa.gov.au>) from April 2013 until February 2015 (Abdul Wahab et al. 2017). During the course of the operations, it was expected that dredging activities would generate about 30 Million m<sup>3</sup> of dredge spoil which would be relocated to dredge material placement sites (spoil grounds). The dredging of the sea floor generally involves removing large amounts of bottom sediments where larger and heavier sediments settle rapidly while the fine sediments remain in suspension for a longer period, but eventually settle with occasional resuspension from wind-driven currents.

Sediment samples from the field sites in Pilbara waters were collected in October 2013, June 2014 and July 2015 field campaigns which were jointly undertaken by Curtin University, the Department of Parks and Wildlife (DPaW), the Australian Institute of Marine Science (AIMS) and the Commonwealth Scientific and Industrial Research Organization (CSIRO) (Fearn et al. 2017b). Figure 1 shows the field sites from which samples were collected and the general area where dredging activities were carried out during the course of the activities. Some samples were collected by divers, and some were extracted from core samples. Figures 2 and 3 show localised maps of specific sampling sites. In all cases efforts were made to collect only the top (surficial) fine sediments which would represent sediment that had recently been dredged and settled, although in reality all samples included a proportion of large particles (including sand, small stones and shell fragments).

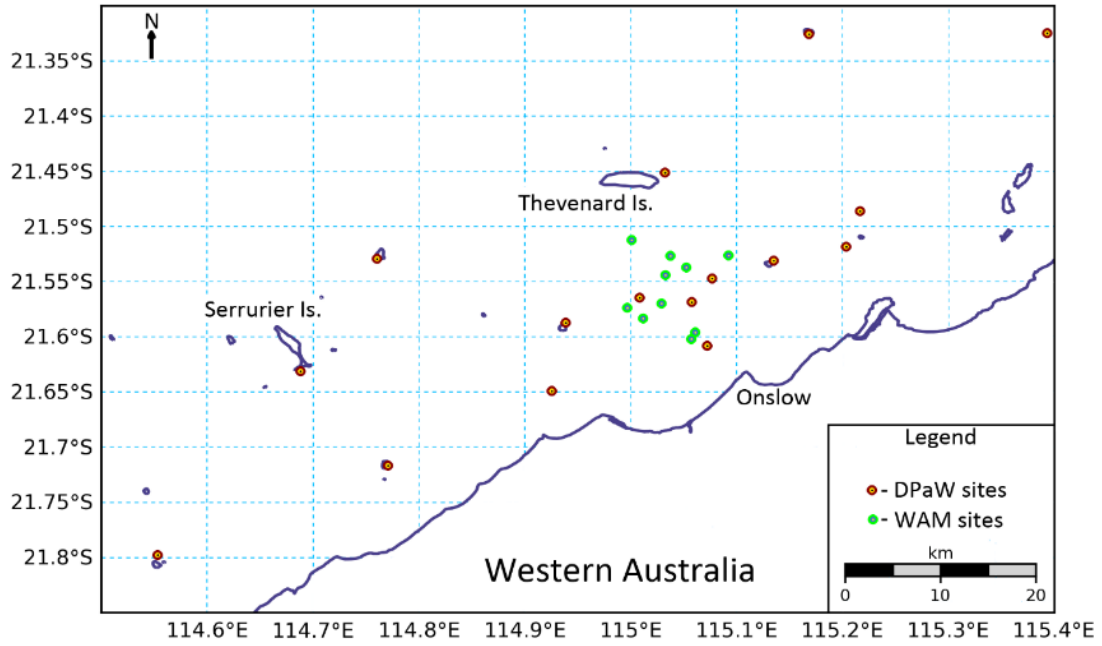


Figure 1. Field sites (Pilbara coast around Onslow, Western Australia) where sample sediments were collected during the 2015 field campaigns. WAM in this figure corresponds to AIMS sites.

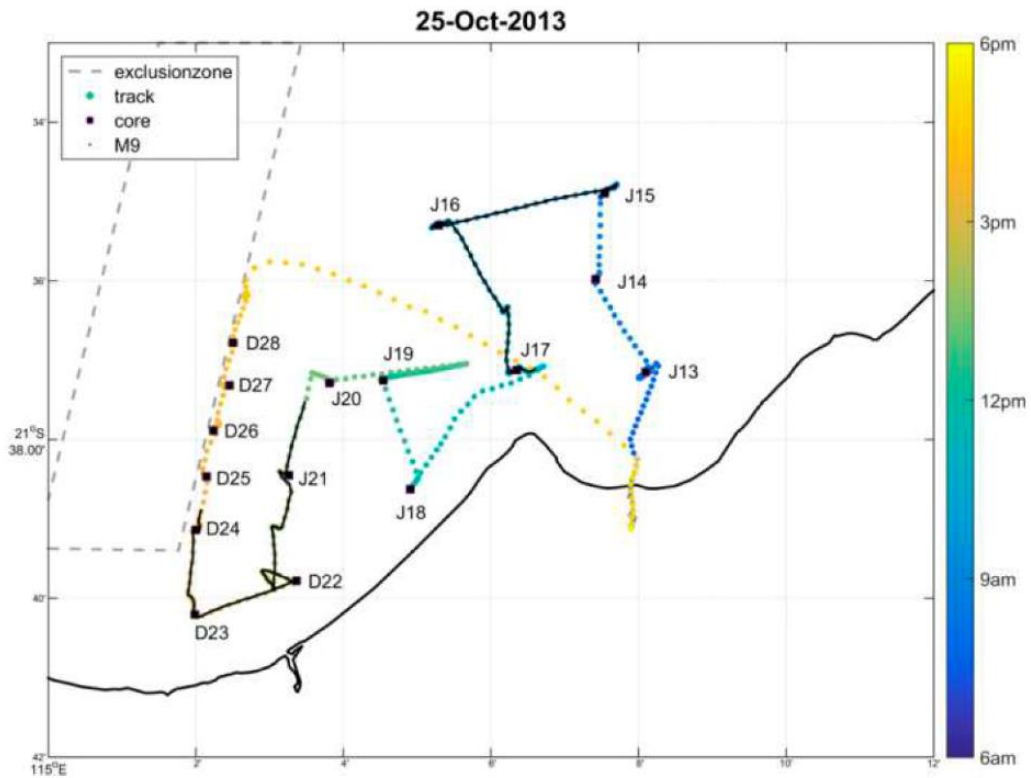


Figure 2. Locations of field survey sample sites for 25 October 2013. Dredge operations occurred within the exclusion zone. Sediment samples from selected sites were analysed in this experiment (see Table 1)

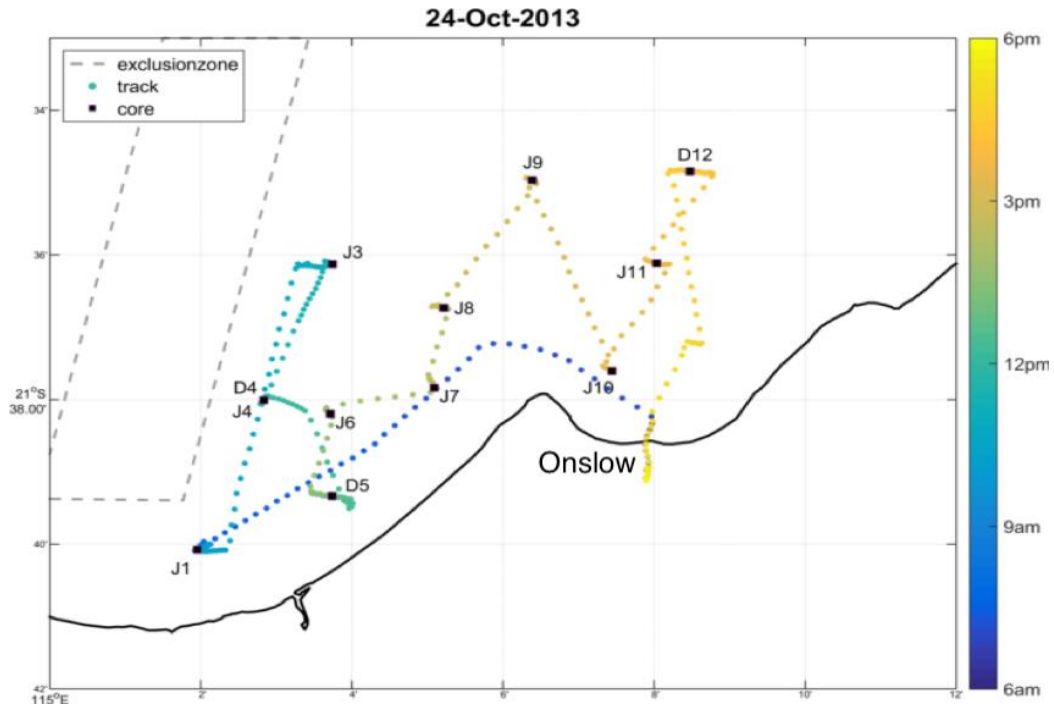


Figure 3. Locations of field survey sample sites for 24 October 2013. Dredge operations occurred within the exclusion zone. Sediment samples from selected sites were analysed in this experiment (see Table 1).

## 2.2 Experiment Design and Data Processing

### 2.2.1 Experiment Design

The experiment was conducted using a large, 1.66 × 1.51 m fibreglass tank in the aquatic laboratory of Curtin University where optical instruments were positioned such that contamination of detectors due to light sources from neighbouring instrument was avoided (Figure 4). The tank was also covered in black plastic to reduce ambient light. The tank system included a stirrer constructed by mounting a paint stirring attachment to a 24V 300 W DC motor by a shaft such that the stirring propeller was just above the bottom of the centre of the tank. The stirrer was powered by a variable voltage power supply which was essential to maintain the rotational speed of the propeller at a level to allow the sediments to remain in suspension without creating water vortices which might influence the optical measurement of instruments or cause inhomogeneous concentrations throughout the tank. The larger particles included in the samples (sand, small stones and shell fragments) fell out of suspension soon after addition of sample portions.



Figure 4. Tank and Optical Instruments (LISST 100X, acs-176, CTD with attached NTU sensor and HydroScat-6) in an experimental configuration. The image was taken after the experiment had been completed and the turbid water was being drained from the tank.

### 2.2.2 Experiment Procedure

The tank was filled with 5  $\mu\text{m}$  filtered sea-water and all instruments were cleaned before placing each in their designated places as shown in Figure 4. The stirrer was then turned on and allowed to run for 5 minutes before starting measurements. The instruments were run for at least 3 minutes to collect the ‘clean’ water measurements.

Sediment samples (see Table 1) were divided into 10 or less portions and mixed with seawater in an effort to divide the sample into approximately even portions. A single portion of sediment sample was then added to the tank. Instrument outputs were monitored in real-time to observe the uniformity of data. Typically, a period of approximately 1 minute was required for the water to mix well and for the measurements to stabilize. The water was then allowed to mix for 2–3 minutes before water samples were taken, then an additional 2–3 more-minutes of instrument readings were taken. This process was repeated for each additional portion of sample added until all portions were exhausted. The instruments were then all stopped and taken out of the tank for downloading data, cleaning and calibration if required. The process was repeated for each unique sample listed in Table 1.

Water samples were collected using 3  $\times$  1 L bottles and TSS determined gravimetrically. Briefly, the samples were filtered through Whatman GF/F filters (47 mm diameter, nominal pore size of 0.7  $\mu\text{m}$ ) using a low vacuum pressure and flushed using 50 mL of distilled water to remove the residual salt. The filter pads were stored in a cool dry place before being dried in an oven for 24 hrs at 60  $^{\circ}\text{C}$  and repeatedly weighed using an electronic mass-balance with a precision of 0.001 mg until a tolerance weight limit of 0.01  $\text{mg L}^{-1}$  was achieved.

## 2.3 Instrumental and Data Processing

### 2.3.1 SBE 19 plus SeaCAT

A SBE 19plus SeaCAT profiler (Sea-Bird Electronics) with attached Seapoint turbidity sensor was used to measure the conductivity, temperature, pressure and turbidity. The CTD and turbidity sensors were used in profiling mode and switched ‘on’ or ‘off’ using a magnetic switch at the start and the end of each new sediment sample. The CTD sampled at 1 Hz and data were converted to salinity, temperature, depth and turbidity (NTU) following the standard data processing protocol implemented in the SBE Data Processing software.

Sampling times were collated and time series of NTU plotted for each sample to identify periods of approximately 4 minutes where NTU concentration had stabilized after addition of each sediment sample portion.

### 2.3.2 WetLabs ac-s

The WetLabs ac-s used in this experiment is a hyperspectral absorption (a) and attenuation (c) meter with 25 cm path length flow cells. The ac-s provides measurements of absorption and attenuation at 80+ wavelengths in the range of 400–730 nm at 4 nm resolution. The ac-s with a 25 cm path length was designed for use in ‘clear’ water environments and expected to saturate in very turbid waters, but due to the non-availability of a 10 cm path length ac-s, we resorted to using the 25 cm path length instrument with the intention of using only the unsaturated data. The data collection using the ac-s involved first measuring a sample of milli-Q water to establish a baseline for subsequent correction for pure water absorption ( $a_w$ ) and scattering ( $b_w$ ). The pure water corrected data represents the absorption and scattering due to water constituents. The data from the ac-s were merged with the CTD using the time stamps after bin-averaging the CTD and ac-s data to 1 Hz. No time lag correction was applied to the ac-s because the water was considered well-mixed and measurements consistent for the periods of data collection associated with each increase in the TSS concentration. After merging the CTD and ac-s data, the temperature and salinity correction was applied using the relationship from Sullivan et al. (2006).

$$\begin{aligned} c_{mts} &= c_m - (\psi_T * (T - T_{ref})) - (\psi_s * S) - c_w \\ a_{mts} &= a_m - (\psi_T * (T - T_{ref})) - (\psi_s * S) - a_w \end{aligned} \quad (1)$$

Where:  $c_m$  and  $a_m$ , and  $c_w$  and  $a_w$ , are absorption and attenuation coefficients for the ac-s measured calibration data. T and S are temperature and salinity from the CTD and  $\psi_T$  and  $\psi_s$  are temperature and salinity dependence factors from Sullivan et al. (2006).

For the reflective tube scattering correction we used a reference wavelength ( $\lambda_{ref}$ ) of 715 nm, with the assumption that absorption at  $\lambda_{ref}$  is negligible. Thus, using the following formulation of Equation (2), we implemented the scattering effect correction at all wavelengths for the absorption channel.

$$a_t(\lambda) - a_w(\lambda) = a_{mts}(\lambda) - \frac{a_{mts}(\lambda_{ref})}{[c_{mts}(\lambda_{ref}) - a_{mts}(\lambda_{ref})]} * [c_{mts}(\lambda) - a_{mts}(\lambda)] \quad (2)$$

After the correction, the absorption ( $a_p(\lambda) = a_t(\lambda) - a_w(\lambda)$ ) and scattering ( $b_p(\lambda) = c_{mts}(\lambda) - a(\lambda)$ ) represent the absorption and scattering from the constituents in the water. For the data quality control of the ac-s we analysed all the ac-s data and limited the data to values of a (total absorption including pure water) and b (total scattering including pure water) of  $25 \text{ m}^{-1}$  for blue and green wavelengths (400 nm – 500 nm) and  $30 \text{ m}^{-1}$  for red and near infra-red (NIR) IR wavelengths (>500 nm). From the data we observed that blue and green wavelengths saturated faster than the red and NIR wavelengths and TSS limits of approximately  $60 \text{ mg L}^{-1} - 80 \text{ mg L}^{-1}$  were enough to saturate the ac-s scattering channels for blue wavelengths while  $90 \text{ mg L}^{-1} - 110 \text{ mg L}^{-1}$  was required to saturate the red and NIR wavelengths.

The main purpose of the ac-s data was to apply the gamma correction to the HydroScat-6 data.



Figure 5. The ac-s instrument with flow tubes removed.



Figure 6. The HydroScat-6P showing the pairs of light source and sensor windows. Image source: <http://www.hobilabs.com/cms/index.cfm/37/152/1253/1266/index.html>



Figure 7. The LISST-100X.

### 2.3.3 HobiLabs Hydroscat-6

The Hydroscat-6P (HobiLabs: Figure 6) measures the backscattering of light in six spectral channels at  $\lambda = 420$  nm, 442 nm, 470 nm, 510 nm, 590 nm and 700 nm and fluorescence in 2 channels at  $\lambda = 590$  nm and 700 nm. The spectral backscattering coefficient ( $bb(\lambda)$ ) was calculated based on the measured spectral volume scattering function  $\beta(\psi)$  at  $\psi = 140^\circ$  following the expression of Maffione and Dana (1997):

$$b_b(\lambda) = b_{bp}(\lambda) + b_{bw}(\lambda) = 2\pi\chi[\beta(140^\circ, \lambda) - \beta_w(140^\circ, \lambda)] + b_{bw}(\lambda) \quad (3)$$

Where:  $\chi$  is a constant proportionality factor between  $\beta(140^\circ)$  and  $b_b$  for particle scattering. The default value of  $\chi = 1.08$  was used with the pure water values and the correction for salinity after Morel (1974) and Twardowski et al. (2007). HydroScat-6 backscattering measurements, particularly in highly turbid waters, require adjustment (sigma ( $\sigma$ ) correction) because some light is lost to attenuation in the detection volume which otherwise would contribute to the total backscattering signal. The  $\sigma$ -correction uses the parameter  $Kb_b(\lambda) = a(\lambda) + 0.4b(\lambda)$ . For our experiment we had ac-s measurements for lower turbidity samples which allowed us to compute  $Kb_b(\lambda)$  using the  $a(\lambda)$  and  $b(\lambda)$  measurements. However, for the more turbid samples which did not have concurrent ac-s measurements we linearly regressed the TSS measurement and  $a_p(\lambda)$  and  $b_p(\lambda)$  to generate a linear relationship and then used the pure water  $a_w$  and  $b_w$  to determine the total  $a$  and  $b$ , thus enabling estimation of the  $\sigma$ -correction factor.

### 2.3.4 AQUAscatter 1000R

The AQUAscatter 1000R (Aquatec Group) is an acoustic sensor that operates with up to four transducers. For this experiment we operated the instrument with 0.5, 1, 2 and 4 MHz transducers. A total of 57 raw data files were collected. The files were manually started and stopped so the file lengths were not all of equal length and this required an adjustment to data processing software. When the instrument was deployed and operated in conjunction with other acoustic instruments in the tank (during the first few days) there appeared to be some interference. This interference was evident as horizontal lines in the first 23 profiles of channel 1, and all profiles in channel 4. Subsequently the operating procedure was adjusted to operate the different acoustic instruments individually. Data processing was undertaken based on assumptions of constant salinity and temperature and mean particle radius of 140  $\mu\text{m}$ .

### 2.3.5 LISST-ABS

The LISST Acoustic Backscatter Sediment (ABS) sensor (Sequoia) is an acoustic backscatter sensor designed for suspended sediment concentration. The instrument operates at 8 MHz and is reported to operate over more than four decades of sediment concentration, from approximately 1  $\text{mg L}^{-1}$  to 30,000  $\text{mg L}^{-1}$  and relatively

insensitive to change in particle size from 30 µm to 400 µm. The instrument requires calibration to determine TSS.

### 2.3.6 Sequoia Scientific LISST 100X and data processing procedure

The LISST (Figure 7) data were collected at 1 Hz and similar to the data processing applied to the CTD, LISST data were processed to extract samples where total volume concentration stabilised after addition of each concentration. The PSD from the LISST was averaged across approximately 4 minutes for each concentration. From the PSD the total volume concentration, mean and median particle diameter were derived. LISST data were processed assuming spherically shaped particles.

The LISST instrument data processing software produces a PSD described by a particle volume,  $V(D)$  (in  $\mu\text{L L}^{-1}$ ) for 32 particle size ranges. The particle number concentration,  $N(D)$  (in  $\text{count m}^{-3}$ ) is derived by dividing the volume concentration by the volume of an equivalent spherical particle for each size range.

$$N(D) = \frac{6V(D)}{\pi D^3}$$

The PSD may also be described in  $\text{count m}^{-3} \mu\text{m}^{-1}$ , the average number of particles within a given size class of width  $\Delta D$  for a unit volume of suspension,  $N'(D)$  (Qiu et al., 2016).

$$N'(D) = \frac{N(D)}{\Delta D}$$

## 2.4 Data Merging

Data from the CTD and ac-s were binned to every one second from 4 Hz to allow for the temperature and salinity correction. Data from the turbidity meter were also binned to 1 second as well as synchronised with the CTD measurements. The HydroScat-6 data were collected at 1 second frequency so no data binning was performed before inter-comparisons with the ac-s and NTU data. For the case of TSS measurements, we collected triplicate samples for every increment in TSS concentration. The time of TSS sample collection was used as a reference time to bin all other instrumental data to within  $\pm 1$  mins from the reference time. Thus, for example, if TSS from sample S1 was collected at 10:22:00 am then we used all the instrument data within the period of 10:21:00 am and 10:23:00 am. However, if any erroneous measurements, such as saturation or spikes of scattering or backscattering data were encountered these were filtered by comparing with the mean and allowing for a tolerance level of  $\pm 2$  STD from the mean.

## 3 Results

### 3.1 TSS Measurement

TSS concentration data for all samples is tabulated in Appendix A. From the 19 different sediment samples used (S1–S19, Table 1) the mean TSS concentration ranged from a low of 2.17  $\text{mg L}^{-1}$  to a high of 483.47  $\text{mg L}^{-1}$  (Figure 8) with 13 samples having upper TSS concentrations of  $>80.0 \text{ mg L}^{-1}$ . There were a few samples (S6, S8 and S9) that had TSS upper limits of less than 10.0  $\text{mg L}^{-1}$  because the sample comprised mainly of very large grains that failed to remain suspended in the water, thus leading to a very low TSS value. Further, more than 81% of the TSS concentrations varied by less than 15% from their mean for the triplicate samples while there were 4 samples (seen in sample S3, S4, S9 and S14) that varied by  $>62\%$ . Such variation might be due to the water being not well mixed when the samples were collected.

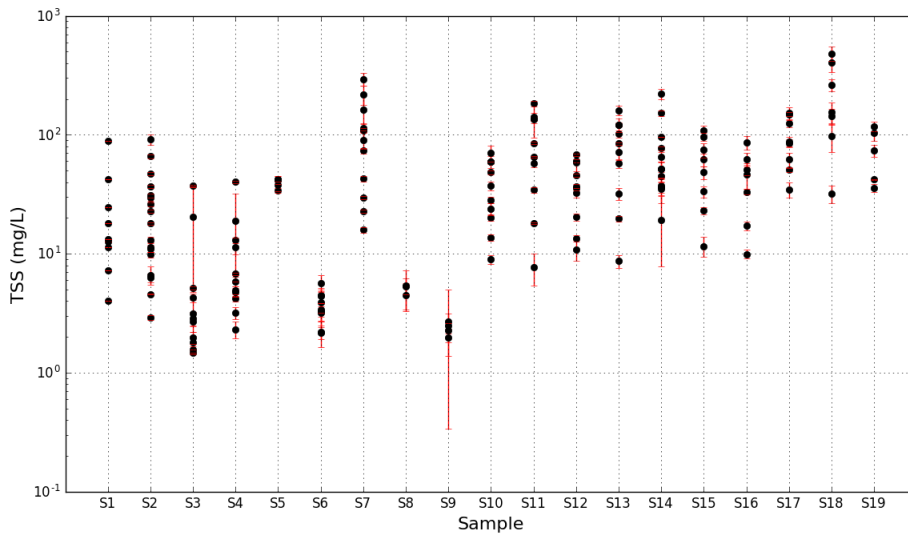


Figure 8. TSS concentrations for each sediment sample. The error bars indicate the standard deviation derived from the mean TSS concentration of each triplicate reading. S1 is missing error bars because only one sample per concentration was collected for the first test experiment. TSS concentration is displayed in logarithmic scale and each black dot represents the mean TSS concentration for each sediment sample triplicate.

### 3.2 ac-s and HydroScat-6 Measurements

#### 3.2.1 Absorption and Scattering Coefficient

The absorption and scattering due to particles,  $a_p(\lambda)$  and  $b_p(\lambda)$ , were studied for how they varied with TSS concentration. Four samples (S2, S11, S12 and S13) were selected to determine the relationship between TSS and  $a_p(\lambda)$  and  $b_p(\lambda)$  because these samples had more data points and spanned a larger TSS range than other sediment samples. The plots of the four samples corresponding to the wavelengths of the HydroScat-6 are shown below in Figure 9 and Figure 10 for  $a_p(\lambda)$  and  $b_p(\lambda)$  respectively. The fit between TSS and  $a_p(\lambda)$  or  $b_p(\lambda)$  is linearly related and the regression coefficient ( $R^2$ ) is greater than 0.7 for all except  $a_p$  at 700 nm and  $b_p$  at 420 nm. Because of the high linearity between TSS and  $a_p(\lambda)$  or  $b_p(\lambda)$  in our samples, we chose to use this relationship to correct the HydroScat-6 data using the sigma correction.

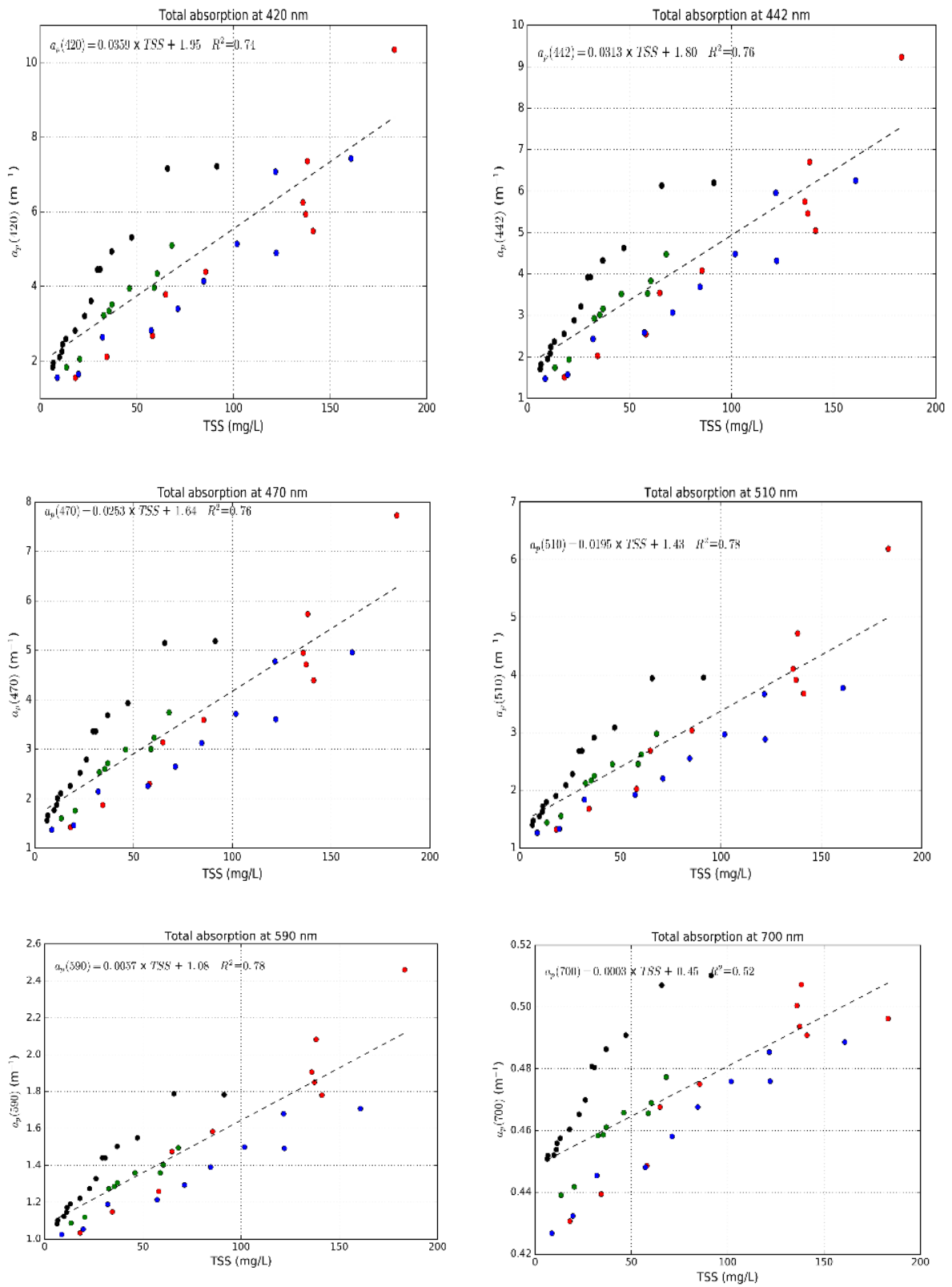


Figure 9. Absorption due to particulates at 420 nm, 442 nm, 470 nm, 510 nm, 590 nm and 700 nm measured using the ac-s for all sediment concentrations. Data associated with each of the four sediment samples are represented by a different colour.

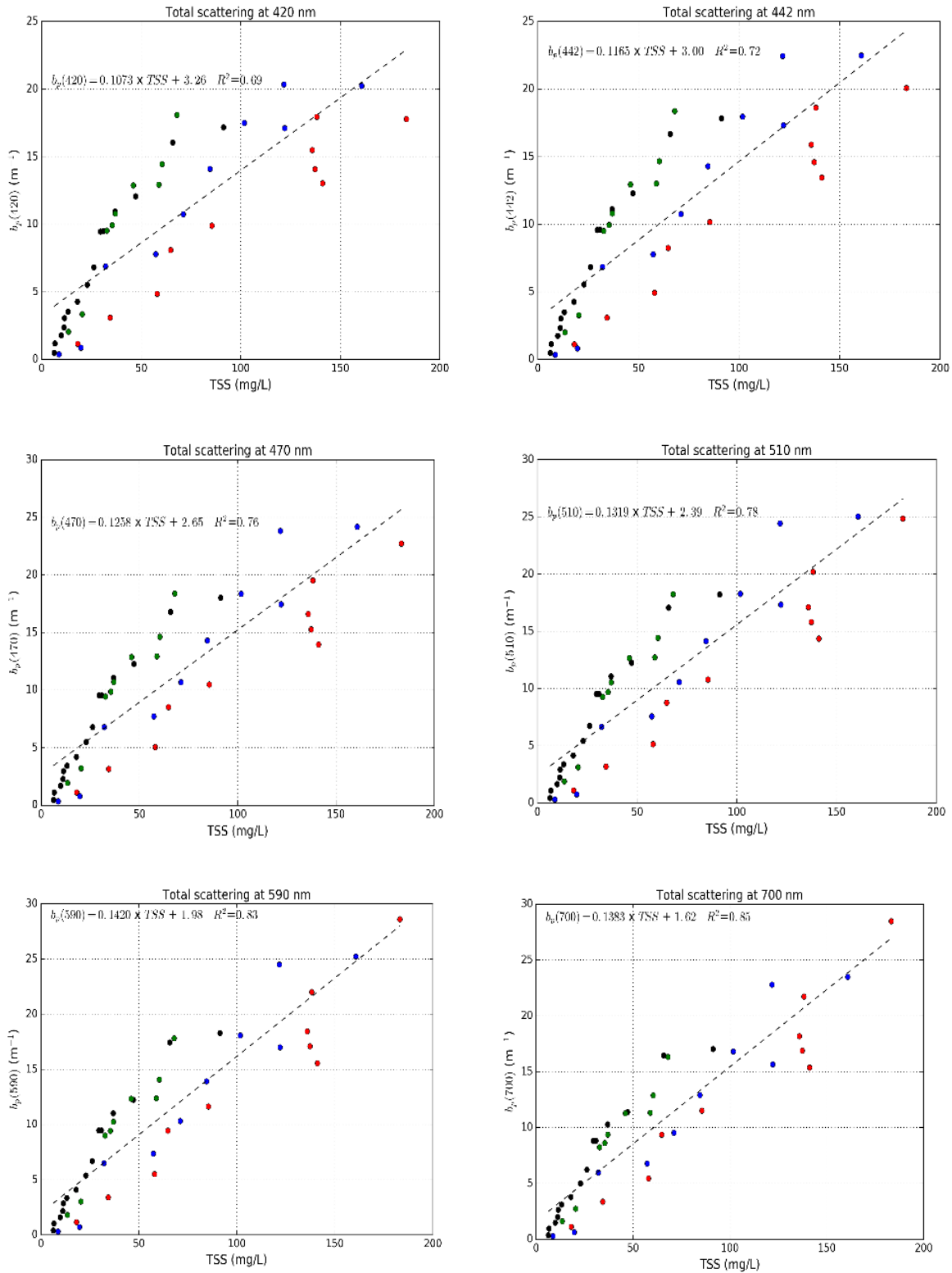


Figure 10. Scattering due to particulates at 420 nm, 442 nm, 470 nm, 510 nm, 590 nm and 700 nm measured using the acs for all sediment concentrations. Data associated with each of the four sediment samples are represented by a different colour.

### 3.2.2 Backscattering coefficient

Figure 11 shows  $b_{bp}(\lambda)$  for three backscattering HydroScat channels (420 nm, 510 nm, 590 nm) for all samples

except for S2, S3, and S10. S2 and S3 were missing HydroScat-6 data while S10 was from the onshore river location, Riverton Bridge in Perth, Western Australia. Also shown in Figure 11 are the  $b_{bp}(\lambda)$  relationships with TSS concentration. The regression between  $b_{bp}(\lambda)$  and TSS was performed using the power function  $b_{bp}(\lambda) = k_1 \times TSS^{k_2}$  where  $k_1$  and  $k_2$  are parameters that are determined from the regression analysis. Two regression analyses were performed: (1) using all available TSS samples at all concentrations, and (2) only using TSS samples less than 100 mg L<sup>-1</sup>. The first regression analysis produced a regression slope greater than 2.0. For the second regression analysis using TSS concentrations less than 100 mg L<sup>-1</sup> we obtained  $k_2$  values of 1.06, 1.22 and 1.34 at 420 nm, 510 nm and 590 nm respectively. The details of  $b_{bp}(\lambda)$  for each individual sample and its relationship to TSS concentration is not included in this report.

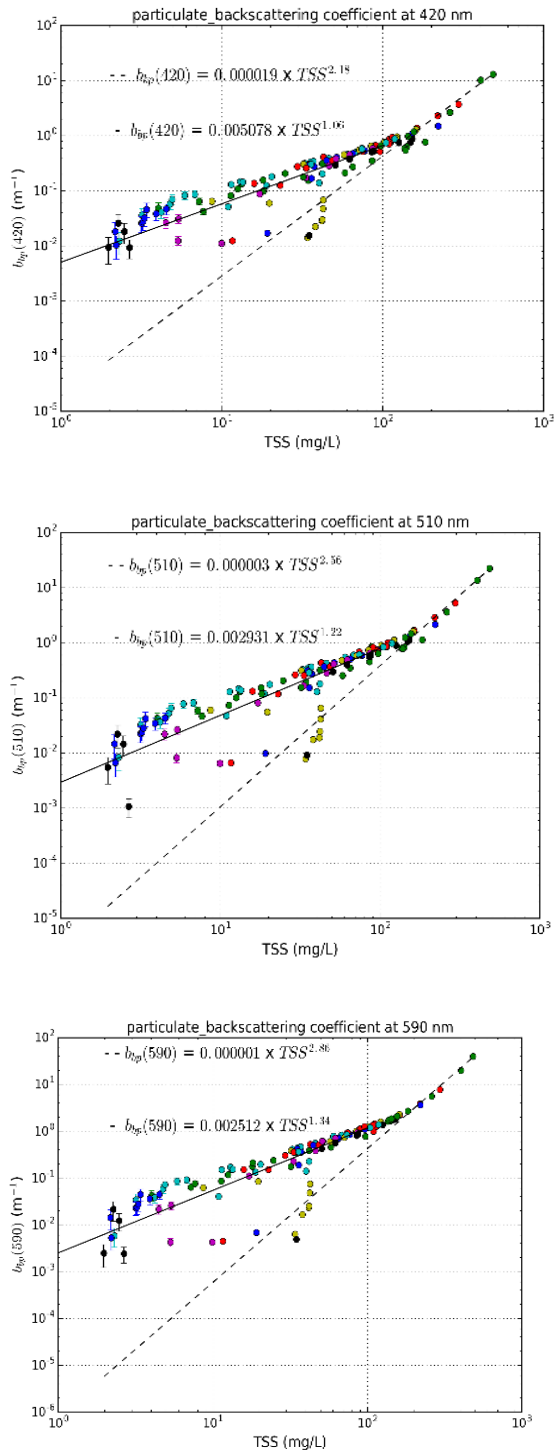


Figure 11. Particulate backscattering at 420 nm, 510 nm and 590 nm for all sediment samples measured using the Hydroscat-6. The regression lines are for all TSS concentrations (dashed lines) and TSS less than 100 mg L<sup>-1</sup> (solid lines). The error bars indicate one standard deviation in backscattering measurement binned at ± 2 minutes.

### 3.2.3 Mass-specific backscattering coefficient

The mass-specific backscattering coefficient,  $b_{bp}^*(\lambda)$ , was examined for sediment samples using the following relationship at all available HydroScat-6S backscattering channels:

$$b_{bp}^*(\lambda) = \frac{b_{bp}(\lambda)}{TSS} \quad [\text{m}^2 \text{g}^{-1}] \quad (4)$$

The mass-specific backscattering coefficients are presented in Table 2.

Table 2. Mass-specific backscattering coefficient ( $\text{m}^2 \text{g}^{-1}$ ) derived for sediment samples in Table 1. The values in brackets are one standard deviation derived from  $b_{bp}^*(\lambda)$  at different TSS concentrations for one particular sample.

ID	bbp* (420)	bbp* (442)	bbp* (470)	bbp* (510)	bbp* (590)	bbp* (700)
S04	0.0103 (0.0034)	0.0108 (0.0038)	0.0109 (0.0039)	0.0095 (0.0035)	0.0104 (0.0041)	0.0077 (0.0032)
S05	0.0009 (0.0004)	0.0009 (0.0005)	0.0009 (0.0005)	0.0007 (0.0004)	0.0008 (0.0005)	0.0006 (0.0004)
S06	0.0092 (0.0023)	0.0096 (0.0026)	0.0095 (0.0028)	0.0080 (0.0025)	0.0081 (0.0029)	0.0060 (0.0023)
S07	0.0089 (0.0015)	0.0105 (0.0025)	0.0118 (0.0034)	0.0103 (0.0028)	0.0135 (0.0047)	0.0099 (0.0032)
S08	0.0047 (0.0017)	0.0054 (0.0020)	0.0051 (0.0020)	0.0038 (0.0016)	0.0035 (0.0019)	0.0027 (0.0015)
S09	0.0068 (0.0030)	0.0080 (0.0037)	0.0071 (0.0035)	0.0047 (0.0035)	0.0041 (0.0035)	0.0030 (0.0027)
S10	0.0043 (0.0007)	0.0046 (0.0007)	0.0048 (0.0009)	0.0039 (0.0008)	0.0036 (0.0008)	0.0030 (0.0007)
S11	0.0045 (0.0006)	0.0053 (0.0008)	0.0061 (0.0006)	0.0057 (0.0006)	0.0113 (0.0017)	0.0097 (0.0016)
S12	0.0084 (0.0016)	0.0094 (0.0018)	0.0104 (0.0017)	0.0089 (0.0016)	0.0111 (0.0026)	0.0087 (0.0020)
S14	0.0067 (0.0020)	0.0079 (0.0024)	0.0087 (0.0027)	0.0073 (0.0024)	0.0104 (0.0039)	0.0083 (0.0031)
S15	0.0060 (0.0020)	0.0071 (0.0024)	0.0077 (0.0027)	0.0066 (0.0024)	0.0097 (0.0040)	0.0079 (0.0033)
S16	0.0056 (0.0020)	0.0064 (0.0024)	0.0068 (0.0027)	0.0057 (0.0024)	0.0081 (0.0038)	0.0063 (0.0030)
S17	0.0052 (0.0018)	0.0063 (0.0022)	0.0072 (0.0026)	0.0060 (0.0022)	0.0090 (0.0036)	0.0076 (0.0031)
S18	0.0128 (0.0085)	0.0186 (0.0152)	0.0228 (0.0197)	0.0177 (0.0148)	0.0277 (0.0262)	0.0195 (0.0172)
S19	0.0072 (0.0012)	0.0083 (0.0013)	0.0091 (0.0018)	0.0075 (0.0016)	0.0100 (0.0024)	0.0081 (0.0019)

### 3.2.4 The Backscattering probability

The backscattering probability of particulates was computed using the ratio  $b_{bp}(\lambda)/b_p(\lambda)$  at all HydroScat-6 channels for four sediment samples (S04, S07, S12 and S13). Only four sediment samples with available HydroScat-6 backscattering measurements and ac-s measurements were available after quality control and limiting to a minimum of five data points required to produce statistically significant results. Figure 12 shows the  $\tilde{b}_{bp}(\lambda)$  results. The backscattering probability ranged from 0.2 % to a high of 21%. On average, for all the samples S04, S07, S12 and S13 combined,  $\tilde{b}_{bp}(\lambda)$  was  $0.061 \pm 0.027$ ,  $0.069 \pm 0.029$ ,  $0.075 \pm 0.029$ ,  $0.066 \pm 0.027$ ,  $0.082 \pm 0.028$ , and  $0.073 \pm 0.023$  for 420 nm, 442 nm, 470 nm, 510 nm, 590 nm and 700 nm respectively.

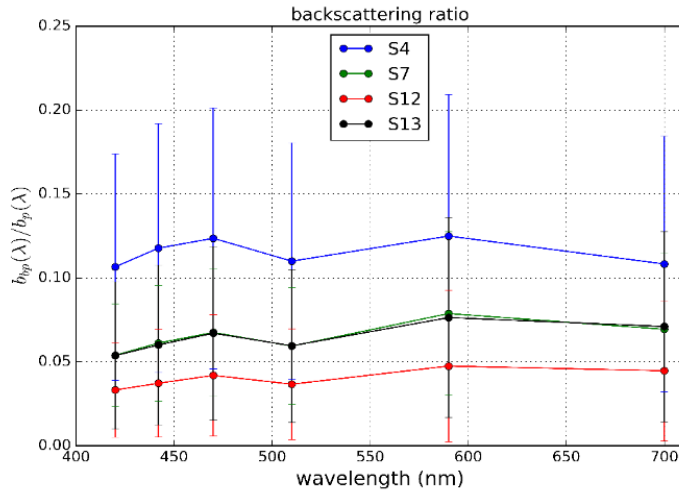


Figure 12. Backscattering probability at different wavelengths for four different sediment samples. Error bars indicate the upper and lower range for each sediment sample at each HydroScat-6 channel.

### 3.2.5 Backscattering spectral slope

According to Morel (1973) the value of the backscattering spectral slope,  $\gamma_{bp}$ , can be used as a proxy for particle size distribution under the assumption that particles are non-absorbing and follow a power law (Antoine et al., 2011). A well-established relationship of backscattering of particulate matter ( $b_{bp}(\lambda)$ ) dependent on the wavelength is given by Equation 5. This Equation was used in calculating the backscattering spectral slope ( $\gamma_{bp}$ ) following a regression analysis between  $b_{bp}(\lambda)$  and wavelength:

$$b_{bp}(\lambda) = b_{bp}(\lambda_{ref}) \left( \frac{\lambda}{\lambda_{ref}} \right)^{-\gamma_{bp}} \tag{5}$$

Where  $b_{bp}(\lambda_{ref})$  is the backscattering at the reference wavelength ( $\lambda_{ref} = 590$  nm). Three different approaches were selected to estimate  $\gamma_{bp}$  with respect to the selection of wavelengths: (1) 420 nm, 442 nm, 470 nm, 510 nm and 700 nm of HydroScat-6 backscattering channels, (2) 510 nm and 700 nm were used, and (3) only 700 nm was used in the regression analysis. The derived gamma parameters are shown in Table 3 for all three regressions. The results from Table 3 show that using only one wavelength (700 nm) produces estimates of  $\gamma_{bp}$  in the range 0.38–1.65. The use of blue and green wavelengths produced some negative  $\gamma_{bp}$  values and values larger than 2.5 which is likely due to significant absorption in those spectral regions.

Table 3. Backscattering slope of particulate matter ( $\gamma_{bp}$ ) derived for sediment samples in Table 1. The values in brackets are one standard deviation derived from  $\gamma_{bp}$  at different TSS concentrations for one particular sample.

Sediment sample	Backscattering slope of particulate matters ( $\gamma_{bp}$ )		
	$\lambda = 510 \text{ nm and } 700 \text{ nm}$	$\lambda = 700 \text{ nm}$	$\lambda = 420 \text{ nm, } 442 \text{ nm, } 470 \text{ nm, } 510 \text{ nm and } 700 \text{ nm}$
S01	0.36 (0.19)	1.54 (0.11)	-0.08 (0.32)
S04	0.56 (0.66)	1.46 (0.59)	0.26 (0.61)
S05	0.49 (0.53)	1.14 (0.31)	0.84 (0.85)
S06	0.70 (0.53)	1.37 (0.73)	0.69 (0.56)
S07	0.03 (0.22)	1.29 (0.25)	-0.60 (0.37)
S08	1.74 (1.67)	0.94 (0.24)	1.83 (1.32)
S09	1.69 (2.16)	1.65 (0.44)	2.85 (1.65)
S10	0.53 (0.18)	0.49 (0.12)	0.80 (0.33)
S11	-0.91 (0.11)	0.38 (0.14)	-1.75 (0.25)
S12	0.02 (0.30)	0.90 (0.16)	-0.36 (0.56)
S13	-0.13 (0.18)	1.04 (0.80)	-0.59 (0.43)
S14	-0.12 (0.70)	0.85 (0.17)	-0.46 (1.13)
S15	-0.04 (1.01)	0.89 (0.47)	-0.40 (1.43)
S16	0.16 (1.07)	1.09 (0.39)	-0.17 (1.37)
S17	0.02 (1.54)	0.72 (0.58)	-0.41 (1.70)
S18	-0.16 (0.22)	1.21 (0.42)	-0.76 (0.53)
S19	-0.26 (0.09)	0.75 (0.05)	-0.56 (0.31)

### 3.3 LISST measurements

Figure 13 shows a sample LISST-derived PSD for sediment sample 10 for a TSS of 37.2 mg L<sup>-1</sup>. From the PSD we can derive mean particle size (PS), modal particle size, TVC of particles, and PSD in terms of particle number. Figure 14 shows LISST-derived mean PSD for all mineral type sediment samples measured in the tank. There is a definite bi-modal distribution, particularly for samples 7 and 16-19. Samples 13 and 15 do not display such a pronounced peak in PSD for larger particles but do display similar peaks to the bimodal samples for small particles. Samples 3, 4, 6, 8 and 9 appear bi-modal but quite jagged. Samples 5 and 12 are less similar to the strongly bi-modal PSDs. Samples 3, 5, 8 and 9 are all characterised by total volume concentrations less than 4  $\mu\text{L L}^{-1}$ . Samples 3-6, 8 and 9 listed as non-CSIRO sites (see Table 1) and were collected in 2015 (all other Onslow field samples were collected in 2013). Sample 12 was collected from close to the Ashburton River mouth.

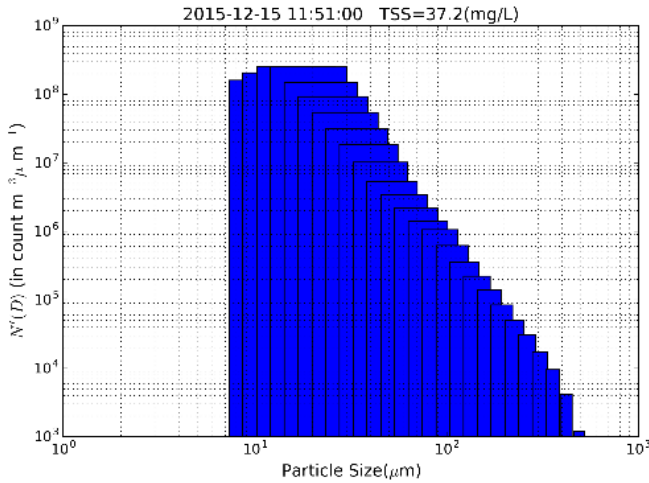


Figure 13. LISST derived PSD for sample 10 at a concentration of 37.2 mg L<sup>-1</sup>.

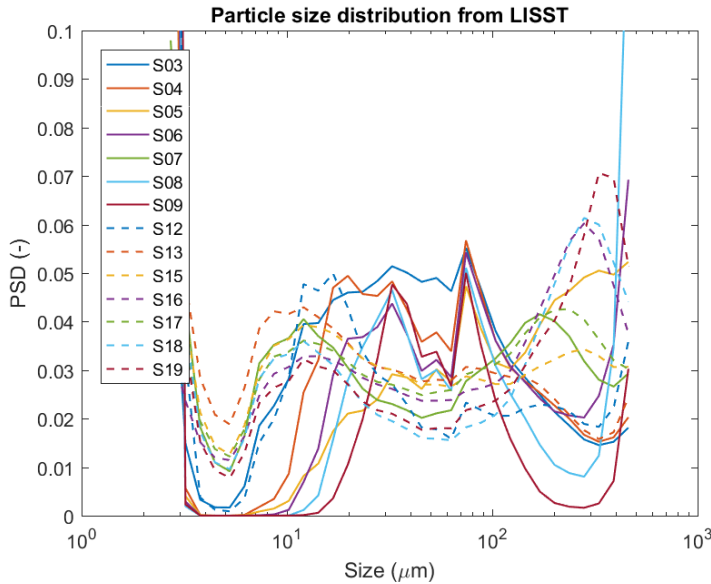


Figure 14. LISST-derived mean PSD for sediment samples collected in Onslow and resuspended in the tank (see Table 1 for sample locations).

The PS and TVC from the LISST 100X is shown in Table 4. The PS shown in Table 4 is the mean PS of each sample across all TSS concentrations. From the mean PS of each sample we observe that sample S10, corresponding to the Riverton Bridge sample in Perth, has the highest mean PS of 169 μm while the smallest mean PS of 11.2 μm belongs to sample S09 which is from the Ashburton Island NE (very close to the Island). The mean PS for the remaining samples ranged within 19.8–55 μm. The LISST failed to produce any reliable measurements above a TSS concentration of 142.9 mg L<sup>-1</sup>

Table 4. Mean particle size (PS) derived from LISST PSD data.

ID	S3	S4	S5	S6	S7	S8	S9	S10	S11	S12	S14	S15	S16	S17	S18	S19
PS (μm)	33.1	29.8	49.3	34.5	33.7	29.4	11.2	169	35.9	19.8	25.3	35.5	55	40.6	45.9	42.9
PS Err (μm)	5.3	4.8	19	5.3	6.5	5.4	3.1	9.5	6.2	1.5	2.1	11.6	13.6	7.1	10.9	8.6

Figure 15 shows the TVC from the LISST and TSS concentration for S10, S11 and S(OTHER) which is all other sediment samples combined. S10 and S11 were from different locations; S10 was from the Riverton Bridge while S11 was from Credo, inland south Western Australia. All samples show strong linear relationships between TVC and TSS but the linearity slope is different for each. S10 TVC increases with a slope of 2 while S11 and others (combined) show slopes of 0.64 and 0.48 respectively. The inverse of the slope from the TVC vs TSS relationship gives particle density, thus the particle density of S10 is less than S11 and S(OTHER) samples. The density of the three sediment groups is  $0.48 \text{ g cm}^{-3} \pm 0.06 \text{ g cm}^{-3}$ , and  $1.44 \text{ g cm}^{-3} \pm 0.38 \text{ g cm}^{-3}$  and  $1.98 \text{ g cm}^{-3} \pm 0.28 \text{ g cm}^{-3}$  for samples S10, S11 and S(OTHER) respectively.

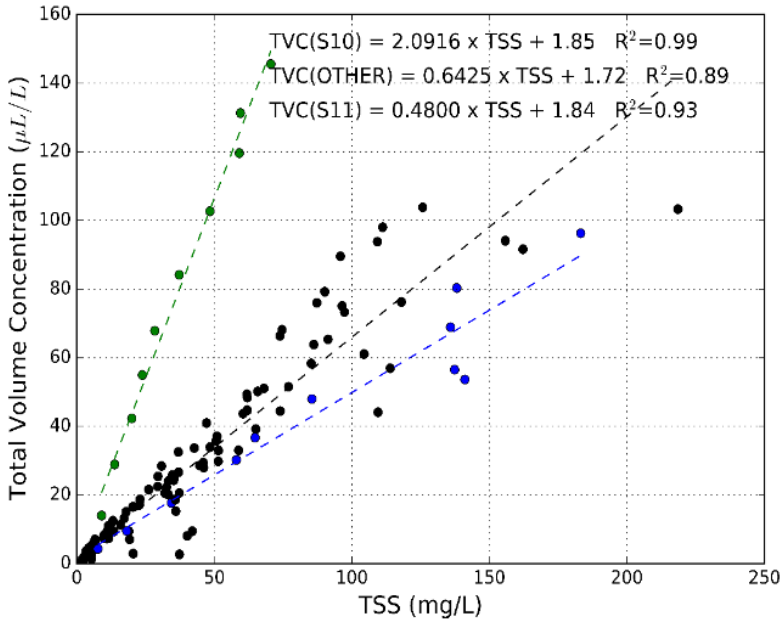


Figure 15. Total volume concentration against TSS concentration plot for three sediment types, S10 (green), S11(blue) and S(OTHER) (black) which is a combination of other samples from Table 1. The inverse slope represents particle density, showing S10 had the lowest density and S11 the highest density.

### 3.4 WetLabs Turbidity Meter

The complete set of NTU time series data is shown in Appendix B. A strong linear relationship was observed between turbidity and TSS concentration for all sediment samples. Figure 16 shows the relationships between turbidity and TSS concentration for two different sample types, S10 and S(OTHER). The turbidity caused by mineral-like S(OTHER) sediment samples increased  $\sim 0.41$  the rate of TSS concentration while turbidity caused by S10 only increased by  $\sim 0.15$  the rate of TSS concentration. Two turbidity and TSS concentration linear relationships were determined for S(OTHER) because of the large range in TSS concentrations ( $\sim 483 \text{ mg L}^{-1}$  upper limit) and because of the sparse data above  $\sim 300 \text{ mg L}^{-1}$ . Figure 16(a) shows the regression for all available TSS concentrations, producing a higher regression coefficient ( $R^2 = 0.98$ ) which might be due to sparse data at the upper limit of TSS concentration that is changing the slope in favour of a tighter fit between turbidity and TSS concentration. Figure 16(b), which shows the relationship for TSS less than  $100 \text{ mg L}^{-1}$ , has  $R^2 = 0.76$  and a higher gradient. One could argue for fitting a curve to such data.

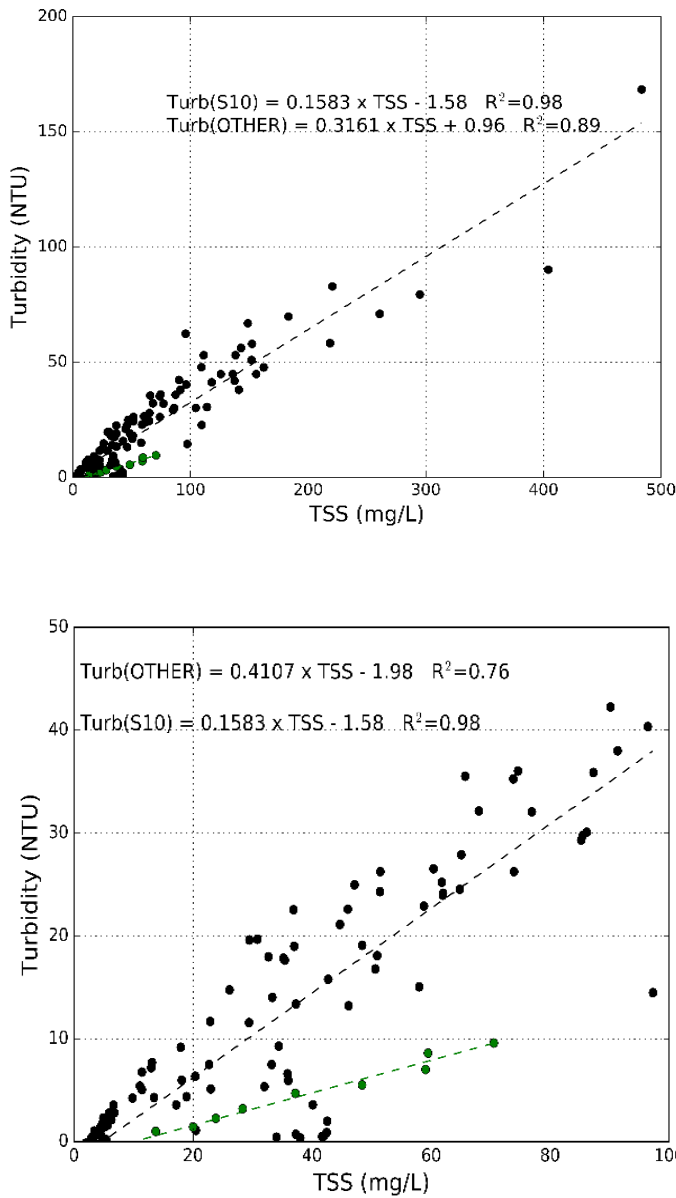


Figure 16. Turbidity and TSS concentration plots for two sediment types, S10 (green) and S(OTHER) (black : a combination of all other samples from Table 1) for (a) the whole TSS range and (b) TSS < 100 mg L<sup>-1</sup>.

It is usual for NTU sensors to be calibrated to provide estimates of TSS by determining relationships between TSS and NTU. All the TSS and NTU data were used to determine a gradient for each set of samples as well as a ratio of TSS to NTU. Figure 17 shows the regression of TSS against NTU as measured by the OBS instrument for sample 19. Appendix C shows similar plots for all sediment samples. The mean ratio of TSS to NTU for the data plotted in Appendix C is 2.2 with a standard deviation of 0.5. Figure 18 shows the relationship for sample J19 for the Wetlabs ECO NTU sensor. Plots for all sediment samples are displayed in Appendix D. The examples shown here are reasonable examples of the typical strength of the relationships, however some samples were characterised by poorer fits.

Note that the OBS3+ was only utilised for S12 through S19, however the agreement between the OBS3+ and Wetlabs ECO NTU was excellent. The OBS3+ simultaneously measures at high (<2000 NTU) and low range (<500 NTU). Whilst the high range has reduced resolution, agreement between the two ranges was very good. As such to simplify discussion of the relationship between NTU and TSS the Wetlabs ECO NTU data (which is available for all samples) will be utilised.

9th Nov 2016: Cast 1: Sample J19 - CTD\_cast1\_tank\_expt\_09\_11\_2016.cnv

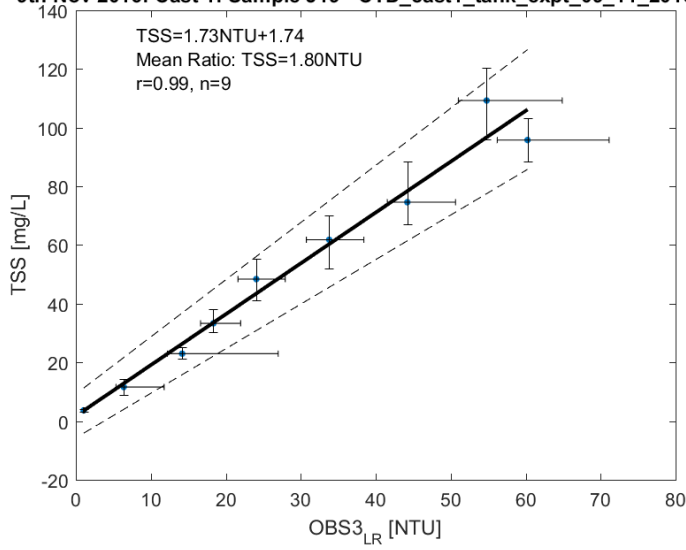


Figure 17. TSS versus OBS regression for sample J19. LR indicates the low range NTU output (0-250 NTU). Both the high range and low range output produced statistically equivalent relationships (not shown)

9th Nov 2016: Cast 1: Sample J19 - CTD\_cast1\_tank\_expt\_09\_11\_2016.cnv

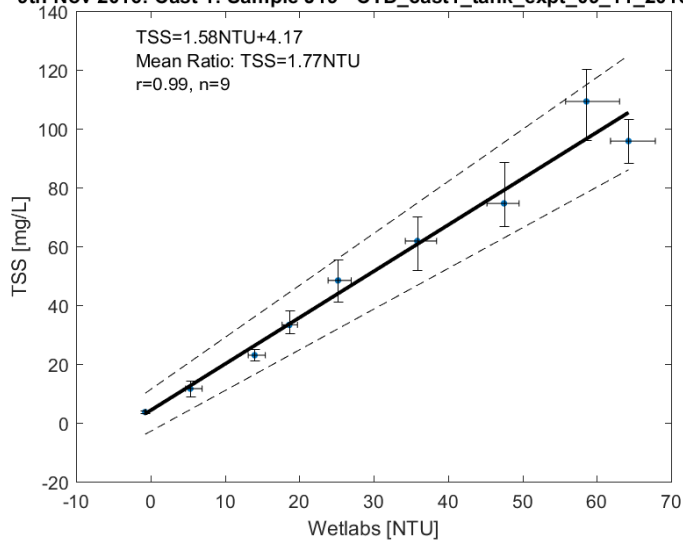


Figure 18. TSS versus ECO NTU regression for sample J19.

Figure 19 below shows the regression of all TSS samples against all NTU (with outliers from samples 18 and 19 removed). The polynomial function in Figure 19 is a slightly better fit than the linear function.

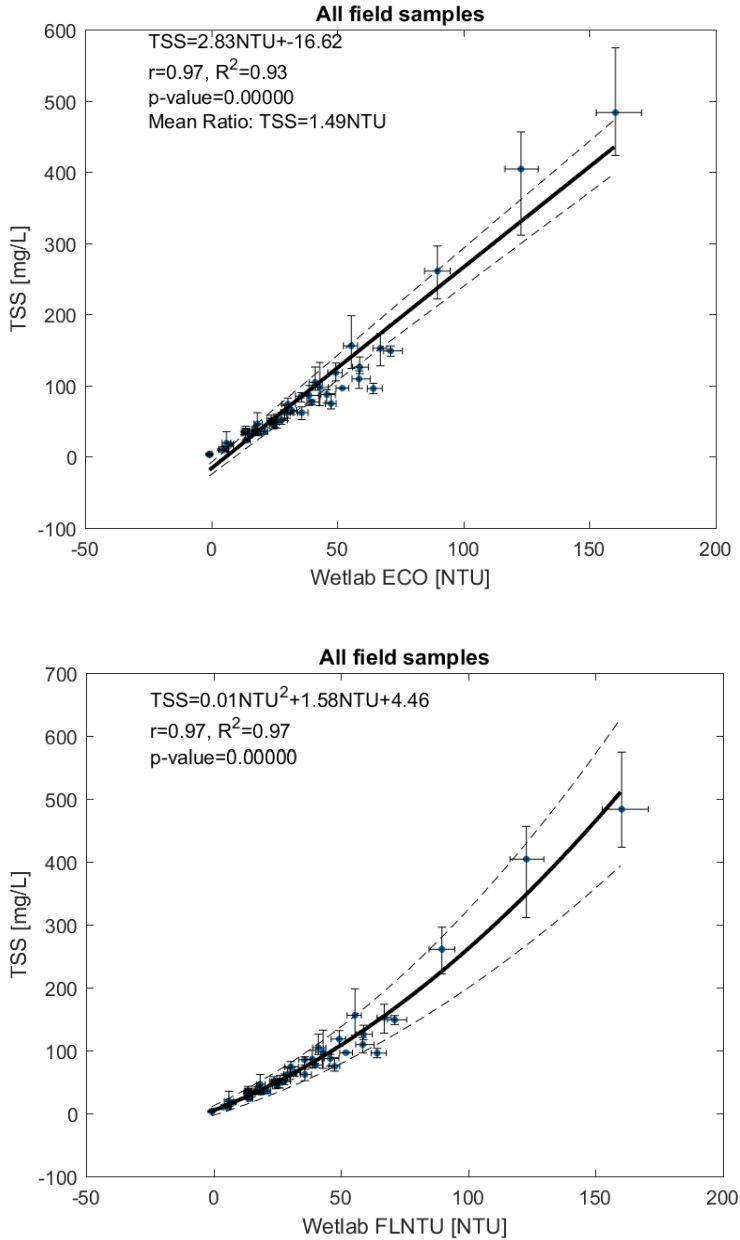


Figure 19. Regression of TSS against NTU for sediment samples collected near Onslow using linear and polynomial functions.

### 3.5 Acoustic sensors

The complete set of data from all 57 AQUAscatter data files is shown in Figure 20. Each panel is for a different transducer frequency (0.5, 1, 2 and 4 MHz). The colours represent acoustic signal strength which can be calibrated to provide TSS.

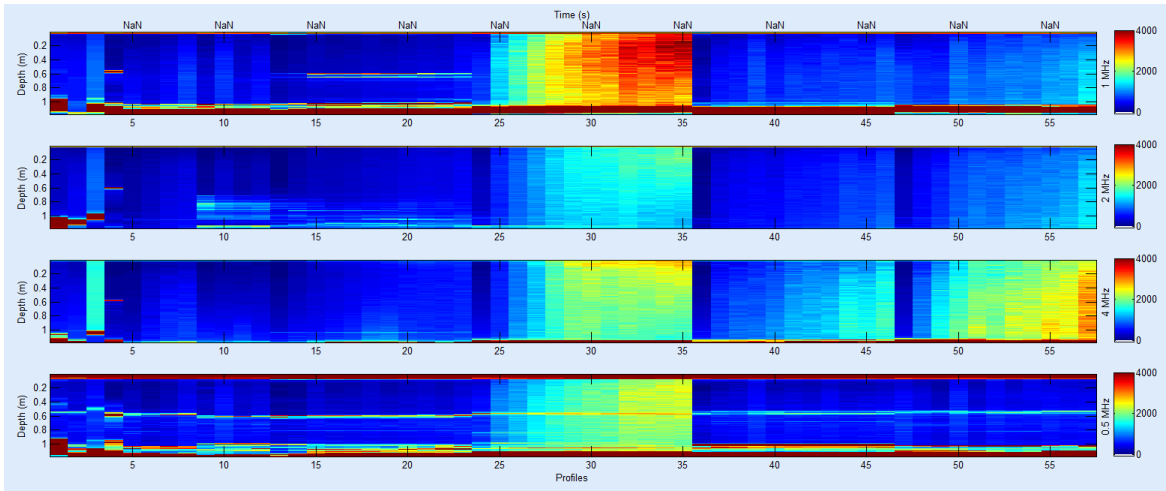


Figure 20. Data from the 57 AQUAscat files plotted in sequence of collection. Each panel from top to bottom is for a different transducer frequency. The vertical axis shows the depth from the transducer. Profile numbers, from left to right, are in order of time collected. Colours indicate acoustic signal strength, representative of TSS.

Only the data sets 24–57 were processed, and the 1 Hz, 2 Hz and 4 Hz channels. Figure 21 shows a summary of the sediment load vertical profiles, representing three series of data for gradual additions of sediment to the tank. The first four depth bins were clipped from all profile data to avoid effects of ringing from the transducers. All files were processed using channels 2 and 3 as this was found to produce the most consistent results for the derived mean grain radius profiles. Data were batch processed at 30 second averages. The acoustic signal strength has been converted to TSS using the manufacturer’s suggested calibration. There are clearly three sections of gradually increasing concentration. Figure 22 shows three series of mean TSS load derived from the AQUAscat data for the same series as represented in Figure 21.

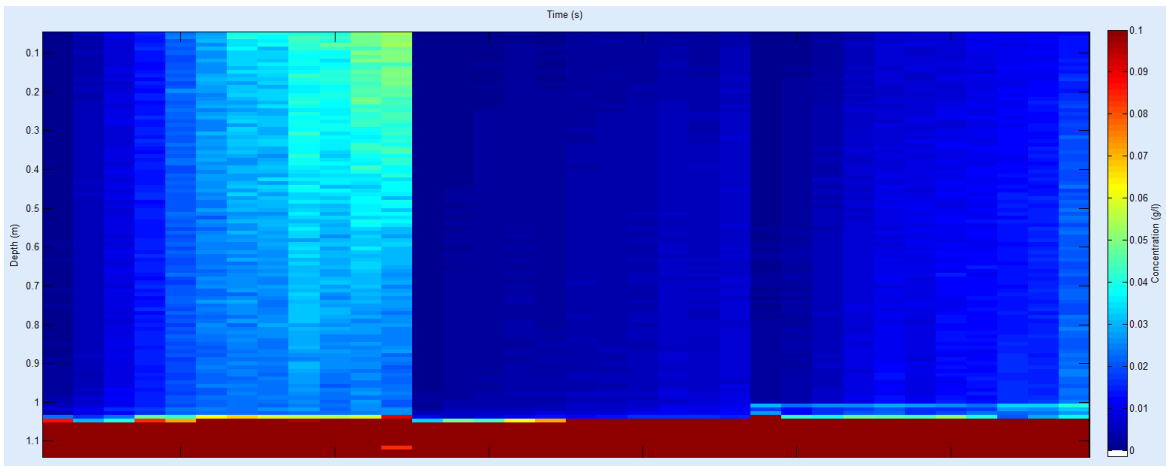


Figure 21. Data for three series of sediment addition as measured by the AQUAscat.

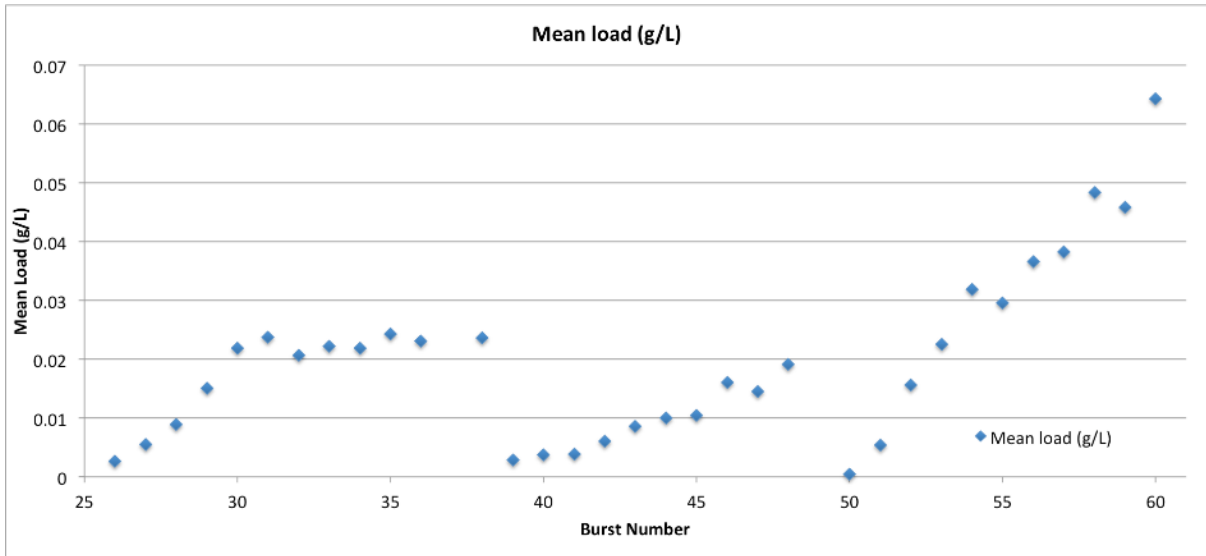


Figure 22. Mean load over each vertical profile derived from the AQUAScat. The three sets of data represent three series of gradual additions of sediment to the tank.

### 3.6 Intercomparison of Instrument Results

#### 3.6.1 Particle size distribution (PSD) parameters and particulate backscattering coefficients

The PSD is expressed as  $N'(D)$  as defined by Equation (6) from Reynolds et al. (2010):

$$N'(D) = N(D) / \Delta D \quad [\text{in count m}^{-3} \mu\text{m}^{-1}] \quad (6)$$

$$N(D) = 6V(D) / \pi D^3 \quad [\text{in count m}^{-3}] \quad (7)$$

where  $N(D)$  is particle number concentration,  $D$  ( $\mu\text{m}$ ) is particle diameter and  $V(D)$  is particle volume concentration (in  $\mu\text{L L}^{-1}$ ) which is derived from the LISST measurements. The blue (420 nm), red (590 nm) and NIR (700 nm) spectral bands were used to determine the relationship between mean particle size (PS),  $N(D)$  and  $V(D)$  and the backscattering coefficient measured from the sediment samples for mineral (S(OTHER)) and non-mineral (S10) samples. The results displayed in Figure 23(a) show a strong relationship between  $b_{bp}(590 \text{ nm})$  and  $V(D)$  for both sample S10 and S(OTHER). For the relationship between  $b_{bp}$  at 420 nm, 590 nm and 700 nm and  $N(D)$  the relationship was weak with  $R^2$  less than 0.5 for all three bands for the S(OTHER) sediment samples, but for the S10 sample the relationship was very strong ( $R^2$  0.99).

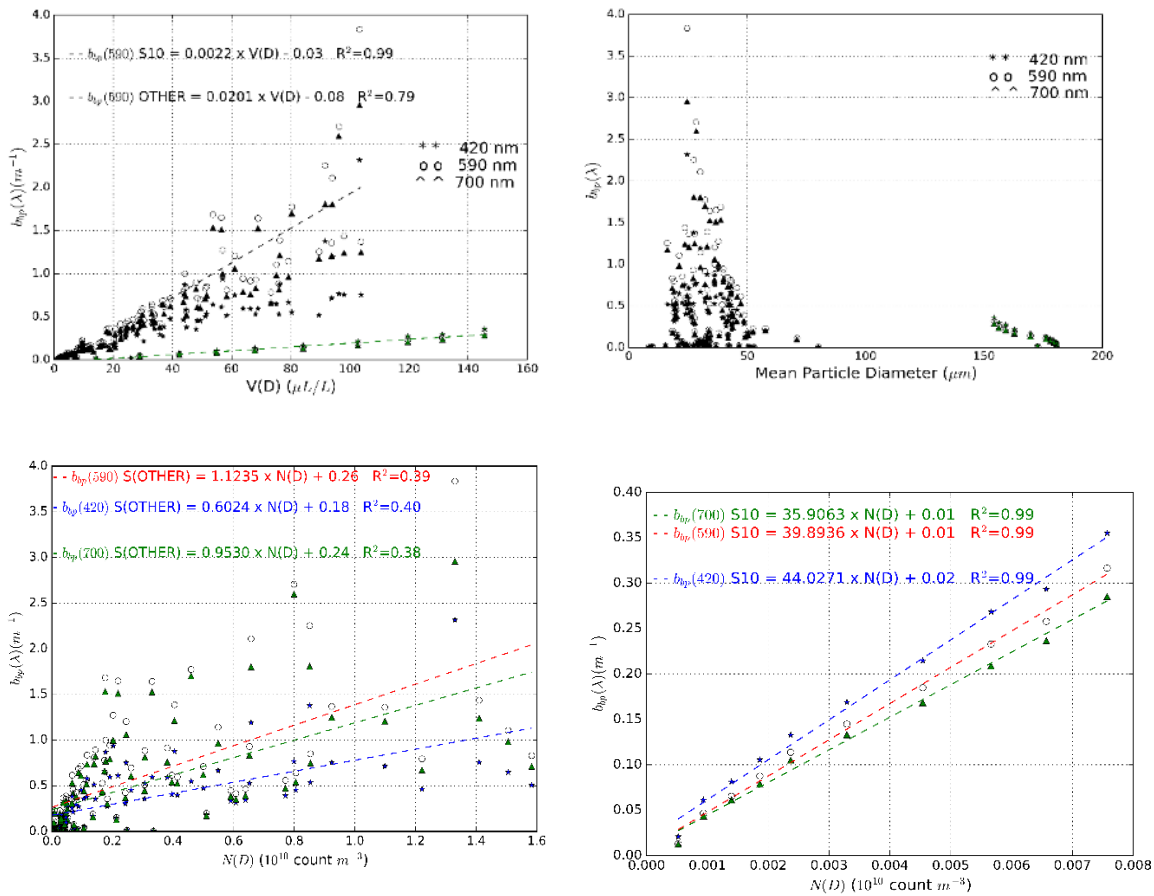


Figure 23. Plot of particulate backscattering coefficient against (a)  $V(D)$ , (b) Mean particle size, (c)  $N(D)$  for all sediment samples excluding S10, and (d)  $N(D)$  for sample S10. Regression analysis was only performed for 590 nm in Figure (a) due to similar variation observed for 420 and 700 nm. For (c) and (d) the regression was performed for all three wavelengths. The symbols in (c) and (d) are diamond for 700 nm, open circle for 590 nm and asterisks for 420 nm.

The slope of the spectral backscattering coefficient of particulate matter,  $\gamma_{bp}$ , was also examined with respect to the mean particle size. Figure 24 shows the mean particle size compared to  $\gamma_{bp}$ . The error bars indicate the range of parameter values for all concentrations for each sediment sample.

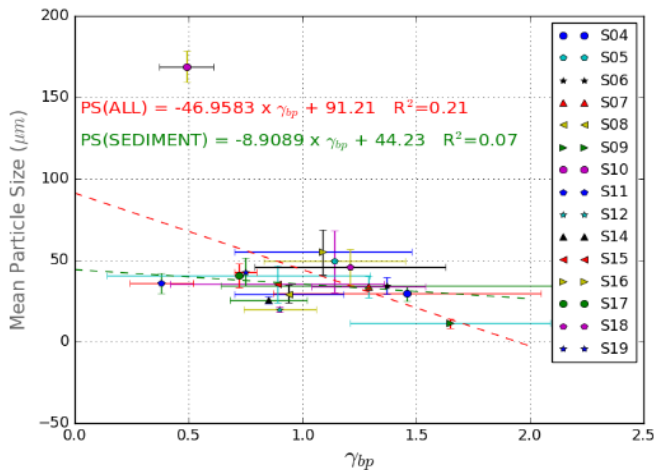


Figure 24. Mean particle size plotted against  $\gamma_{bp}$ . The error bars in both PS and  $\gamma_{bp}$  show the variation with each sample from a range of TSS concentrations.

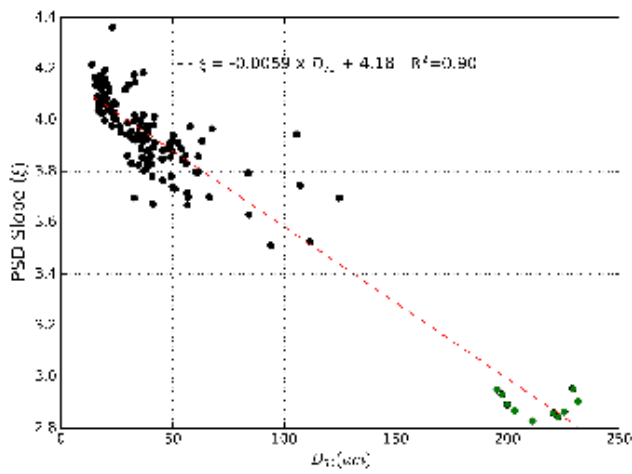
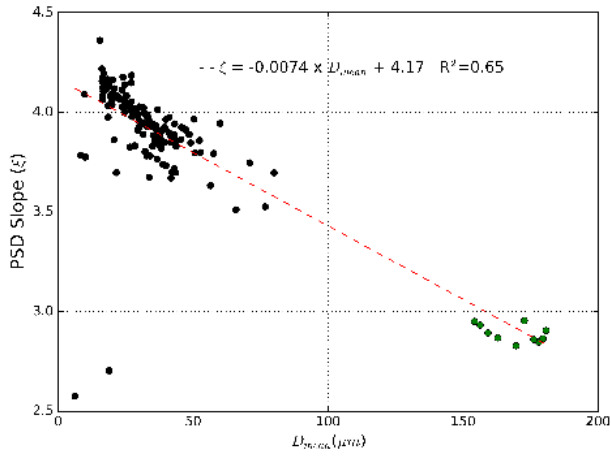


Figure 25. PSD slope versus mean particle size (top panel) and modal particle size (bottom panel) showing data for S10 [green points] and S(other) [black points].

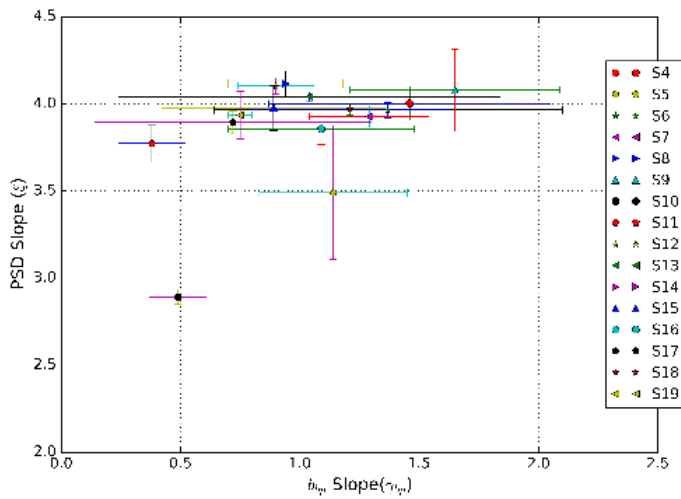


Figure 26. LISST-derived PSD slope versus Hydrosat-derived  $\gamma_{bp}$  for all samples. Error bars indicate the range of values for all concentrations.

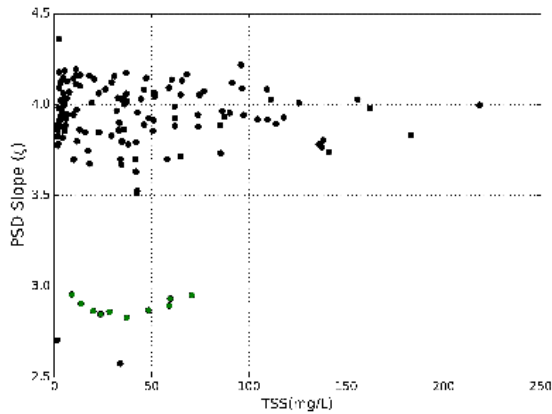


Figure 27. LISST-derived PSD slope versus TSS for S10 [green points] and S(other) [black points].

### 3.6.2 NTU and LISST

Figure 28 shows the relationships between the TSS versus NTU ratio and the modal value of the LISST PSD (a), and the mean size of the LISST PSD (b) for all sediment samples. Figure 28 also shows the relationships between the slope of the TSS versus NTU relationship, and the modal value of the LISST PSD (c), and the mean size of the LISST PSD (d), for all sediment samples.

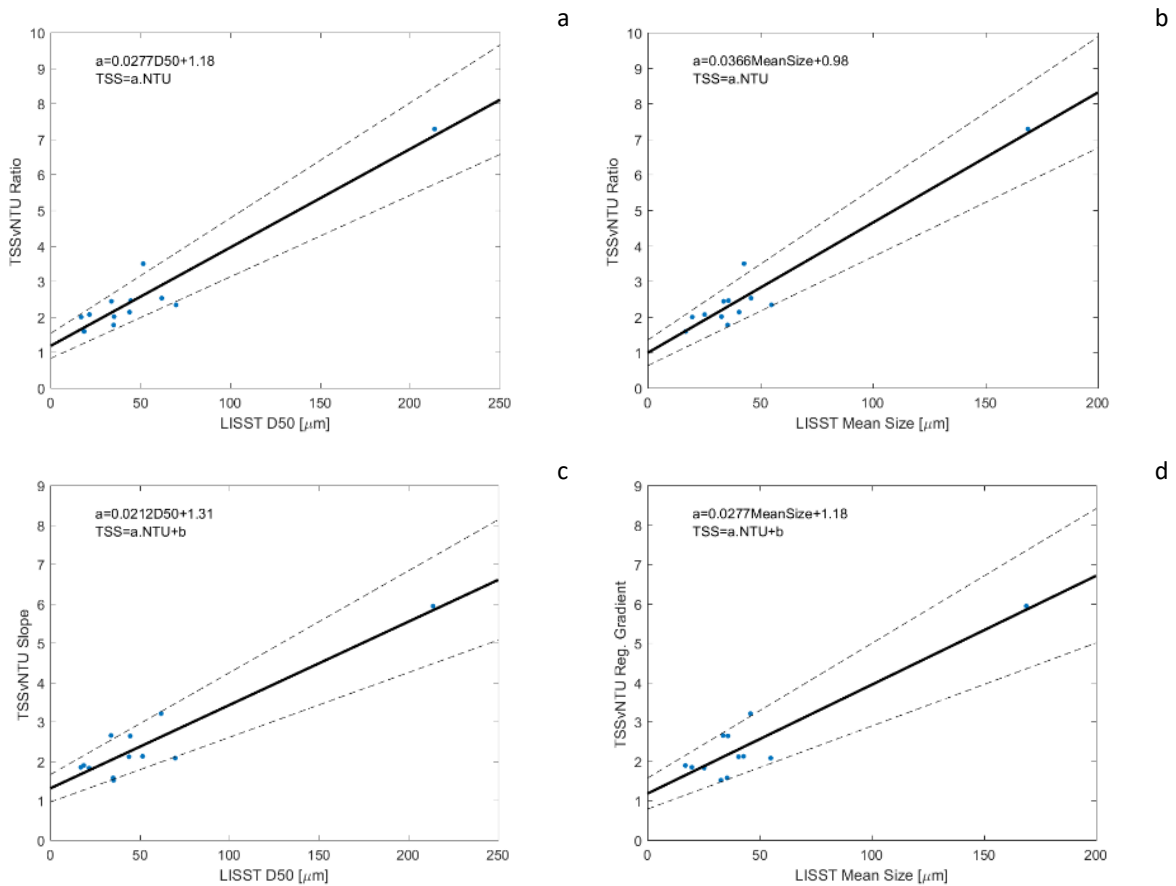


Figure 28. a) TSS vs NTU Ratio versus modal values of LISST PSD, b) TSS vs NTU Ratio versus mean values of LISST PSD, c) TSS vs NTU regression gradient versus modal values of LISST PSD and d) TSS vs NTU regression gradient versus mean values of LISST PSD.

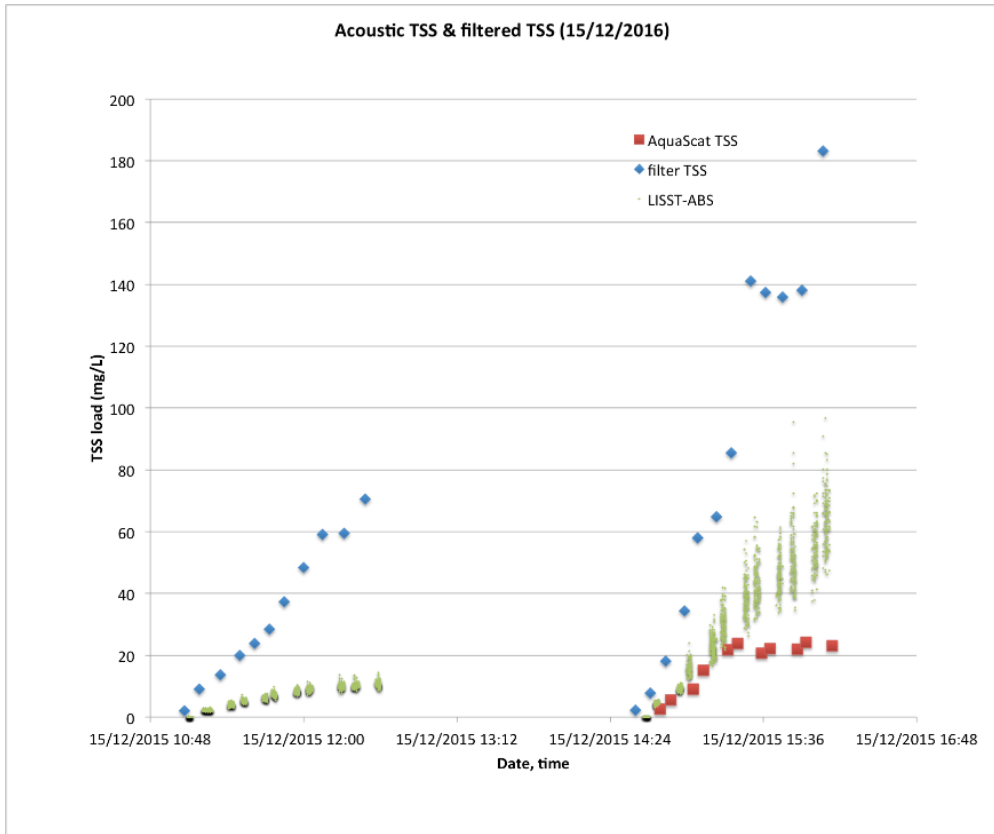


Figure 29. TSS derived from the Aquascat, LISST-ABS and water sampling for data collected on the 15 December 2015.

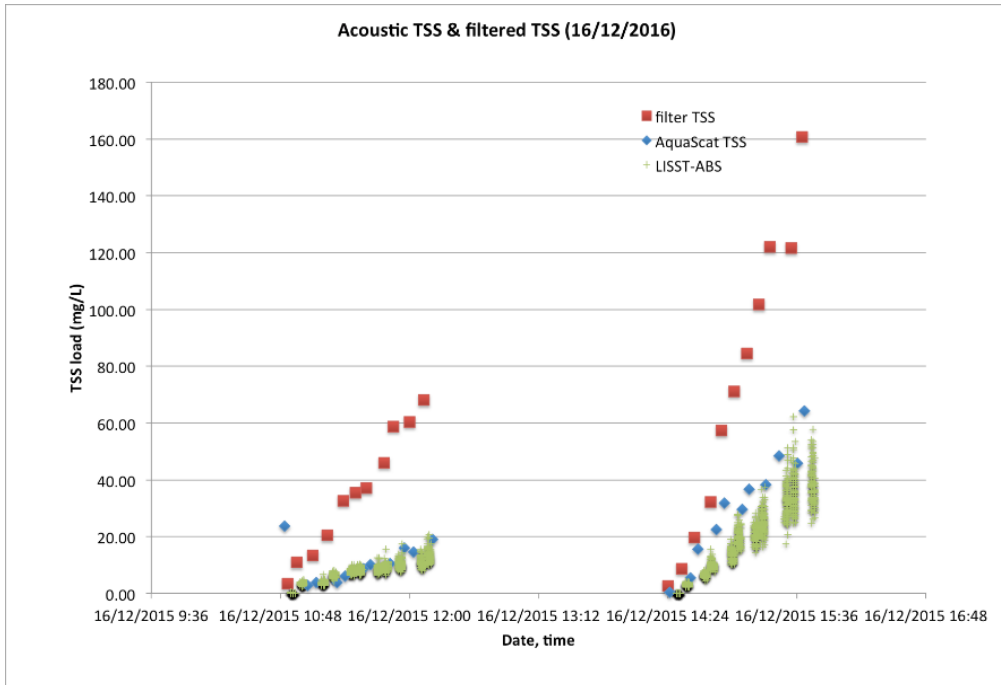


Figure 30. TSS derived from the Aquascat, LISST-ABS and water sampling for data collected on the 16 December 2015.

## 4 Discussion and Conclusions

### 4.1 TSS, NTU and scattering

One of the key questions to be considered for this work is, can sediment samples be collected in the field and subsequently be measured in a tank to determine physical/optical properties representative of the field conditions?

Of particular interest is the relationship between NTU and TSS. Figure 16 and Figure 19(a) do display linear relationships between NTU and TSS; however, limiting the fitting range to  $TSS < 100 \text{ mg L}^{-1}$  does produce a significantly different gradient for the S(OTHER) samples (Figure 16(b)). This suggests that for a large TSS range a non-linear fit might be more appropriate as is displayed in Figure 19(b). The reason for the non-linearity between NTU and TSS is due to the complex optical processes of (multiple) scattering interactions for increasing concentrations of particles. The degree of non-linearity is also a complex mix of effects from factors such as PSD and particle shape. In fact, it is not just the degree of non-linearity affected by the optical characteristics of the particles, but also the NTU to TSS relationship itself. This is evidenced by the significant difference between the gradients of the lines in Figure 16 where the S(10) sample, which contains a larger amount of organic matter, displays a significantly lower gradient.

The ratio between TSS and NTU varies between 1.6 and 2.6 for the field-collected samples. S10 presented the highest ratio of 7.3, once again clearly highlighting the difference between sample sources. The mean ratio between TSS and NTU across all field collected samples was 2.2. The calculation of the mean ratio between TSS and NTU for each individual sample is very sensitive to outliers, in particular for low NTU (due to NTU being the denominator). The ratio is also sensitive to small values, potentially leading to large errors, thus the calculation of a gradient may be considered a better approach for describing the TSS vs NTU calibration. However, the gradient approach usually leads to a non-zero (or non-physical) intercept.

Samples 18 and 19 have two outlier points that significantly affect the estimated ratio. After removal of these points a regression of the TSS v NTU ratio against LISST mean particle size is plotted in Figure 31. Whilst there is a significant amount of scatter relative to the range of the data this does suggest the changes in the relationship between TSS and NTU is due to changes in the PSD where samples are from a similar source.

One aspect of the tank resuspension experiment that has not been investigated fully is the method of mixing or stirring and the energy imparted. The tank experiment is likely to have a much greater shear due to stirring leading to a different particle suspension/settling regime. We could potentially infer that 2.8 would be an upper limit during cyclonic conditions.

Considering all the samples, the slope of TSS v NTU relationship in the tank was approximately 2.2–2.8, compared to 1.1 based on water column samples of dredging plumes in the field (Fearn et al. 2017b).

With respect to the question of using field collected sediment to undertake tank-based measurements for instrument calibration, the results we present here suggest the differences between *in situ* field and tank data are too large to adopt this approach with any confidence. Also, these results suggest that even for a localised sampling campaign in an optically complex environment the TSS vs NTU calibration can vary significantly. It would be wise to collect coincident field TSS data to monitor the NTU calibration and to provide an increased level of certainty to TSS derived from *in situ* NTU sensors.

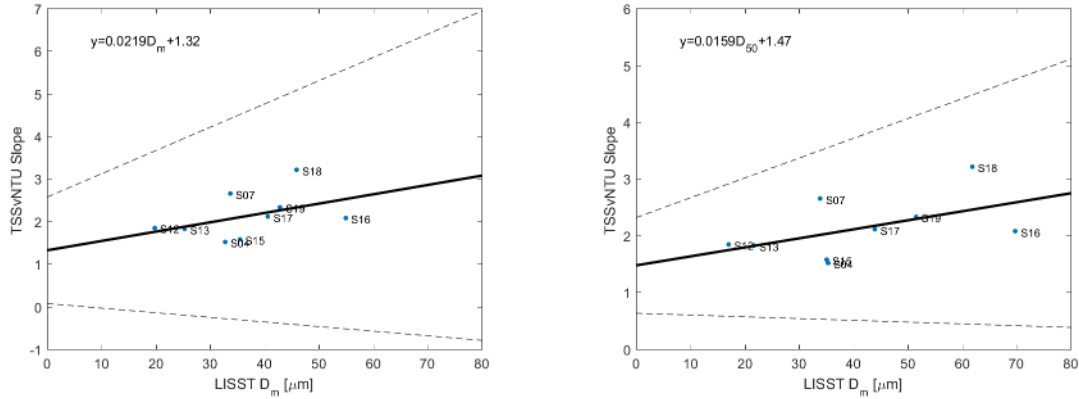


Figure 31. TSS vs NTU slope as a function of LISST mean particle size and modal particle size for field samples collected around Onslow.

From Figure 9 and Figure 10 we observe that  $a_p(\lambda)$  is higher at blue and green wavelengths than red and NIR wavelengths, while  $b_p(\lambda)$  is slightly lower at the blue wavelengths. This pattern of scattering by particulate is expected for mineral rich sediment because minerals are usually high scatterers. We also notice that as TSS concentration increases, the scattering and absorption tend to increase linearly, but there may be a slight dependency on sediment type. Since all the samples being processed were so similar optically we felt it was reasonable to use the relationships between TSS and  $a_p(\lambda)$  and  $b_p(\lambda)$  uniformly across all sediment samples to apply the gamma correction to the HydroScat-6 data.

When using all TSS samples at all concentrations the regression of  $b_{bp}(\lambda)$  against TSS performed poorly in the low TSS region and affected the overall results which can be deduced from the regression slope  $k_2$  which is higher than 2.0. For good correlation,  $k_2$  the regression slope should be close to 1.0 (Reynolds et al. 2016). This shows that the backscattering coefficient of particulate materials is linearly related at lower TSS concentration, but not linear at high TSS concentrations, which has implications for the design of TSS algorithms using simple linear relationships at the aforementioned spectral bands. Note that the semi-analytical TSS algorithm SASM (Dorji et al. 2016) relies on a non-linear relationship between TSS and particulate backscattering. The SASM was found to be quite robust across a large range of sediment types and concentrations and superior to linear algorithms (Dorji & Fearn 2016)

It is interesting to note that the lowest values of  $b_{bp}^*(\lambda)$  occur for S10 (see Table 2), collected from the Riverton Bridge. The sediment sample was observed to include some larger greenish particles, indicating the presence of phytoplankton. The  $b_{bp}^*(\lambda)$  are directly related to  $b_{bp}(\lambda)$  which has an implication in TSS concentration estimation using remote sensing. Understanding the variability of  $b_{bp}^*(\lambda)$  can potentially help better model TSS algorithms and potentially allow remote sensing to estimate different sediment types from space.

The average  $\tilde{b}_{bp}(\lambda)$  results were on the higher side of literature values and this might be partly due to highly turbid waters and the presence of fine sediments or due to data corrections. Whitlock et al., (1981) showed that in turbid waters  $\tilde{b}_{bp}(\lambda)$  were as high as 0.059. The  $\tilde{b}_{bp}(\lambda)$  values from this study are showing higher than this and certainly need to be investigated further as  $\tilde{b}_{bp}(\lambda)$  is potentially important in optical modelling and algorithm development and testing. The wavelength dependence of  $\tilde{b}_{bp}(\lambda)$  shows a dip in  $\tilde{b}_{bp}(\lambda)$  at 510 nm for all the samples considered for  $\tilde{b}_{bp}(\lambda)$  analysis.

#### 4.2 Particle Size Distributions

The dominant characteristic of the PSDs shown in Figure 14 is the bimodal distribution. Also evident is the increasing tails for very small particles, and similarly rising tails for large particles on some PSDs. The size range for the LISST (Type C) instrument is 2.5  $\mu\text{m}$  to 500  $\mu\text{m}$ . Particles outside the size range can lead to increasing tails at the extremes of the PSD (Sequoia 2011). Non-sphericity of particles can also lead to a rising tail, particularly

for the small size classes (Agrawal et al. 2008).

Figure 31 shows LISST-derived PSDs measured in the field near the ocean surface and near the sea floor. Comparing PSDs in Figure 14 and Figure 31 we note that PSDs in the tank are somewhat larger than those measured in the field, and with a much larger fraction in the smallest size bin. However, as noted the large upward tail for the smallest particle sizes may be due to the presence of particles outside the size range of the LISST instrument and/or due to non-sphericity of the particles. The tank data has a larger proportion of small particles (~10-20  $\mu\text{m}$ ) and a peak at ~200-300  $\mu\text{m}$ . Notwithstanding the large variability between all the PSDs displayed, the general shape of the tank-measured PSDs is more similar to the *in situ* near-surface samples than to the near-bottom samples.

It is interesting to note that the PSDs for sediment cores collected in the same locations, but measured in the laboratory by a Malvern Analytical Mastersizer 2000, were bimodal with peaks around 5  $\mu\text{m}$  and 200-600  $\mu\text{m}$  (Figure 31 in Fearn et al. 2017a). Also, the measurement range of the Mastersizer 2000 extended from 0.2 to 2000  $\mu\text{m}$  and not rising tails were evident on any of the PSDs. This suggests the rising tails in the LISST data were measurement artefacts rather than real representations of the PSD.

An explanation for the bi-modal PSD could be that the sampling method was to collect samples from the surface of the seafloor, and it might be the case that fine silt or clay had deposited on an otherwise coarse base material so the samples are representative of both.

The effect of shear mentioned with respect to the TSS to NTU ratio is equally relevant here. We attempted to maintain a constant stirring rate for all measurements so that results are comparable between samples, but it is difficult to determine if the results are representative of those experienced in the field.

The results here do not suggest we have reproduced PSDs representing those measured *in situ*. We have to agree with the view of Mikkelsen and Pejrup (2001) who conclude that laser diffraction instruments “need to be deployed in the field if reliable assessments of natural PSD are to be made”.

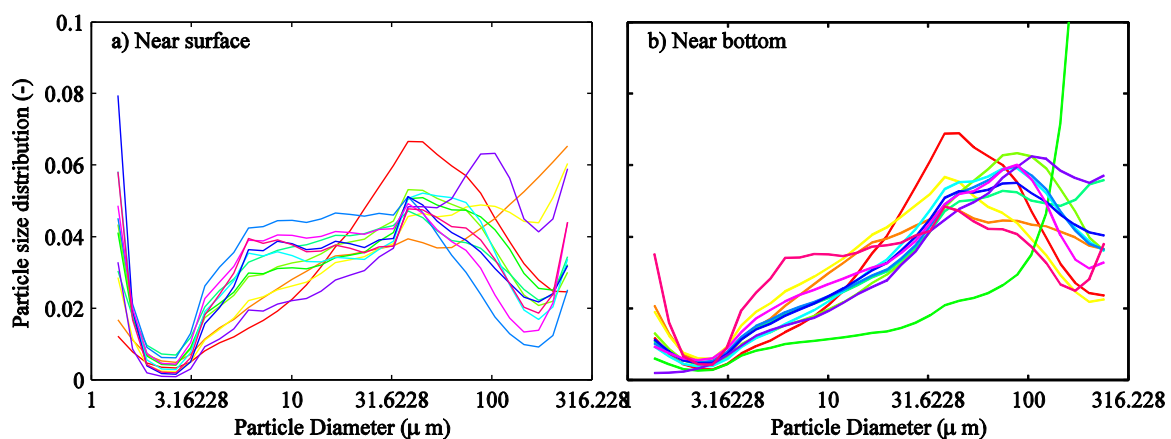


Figure 32. *In situ* particle size distributions at the surface and bottom as measured by the LISST (Figures reproduced from Fearn et al. 2017b).

A common approach to simplifying the description of the PSD is to calculate the slope component of the Jung distribution. This requires converting the LISST derived total volume concentration PSD into a particle count PSD, then fitting a simple power law function to the PSD. The assumption is that the PSD can be well described by a Jung distribution. The strongly bi-modal distribution for the majority of our samples tends to limit the application of the Jung model. We have therefore resorted to comparing the mean particle size and/or the modal particle size to other measurements. The inherent weakness in this approach is that mean (or mode) does not express the distribution of particles across the size spectrum. In fact, we see that for the samples from the dredge region (S(OTHER)), the range of PS is relatively narrow (Table 4). The relationship between TVC and TSS, as shown in

Figure 15, is relatively consistent for all S(OTHER) samples, and the two alien samples, from the Riverton Bridge (S10) and Credo (S11), display distinctly different TVC versus TSS relationships.

The backscattering coefficient,  $b_{bp}(\lambda)$ , should co-vary with the  $N(D)$  and  $V(D)$  in sediment samples in non-absorbing wavelength bands (Qiu et al., 2016). It is interesting to note that there was a strong relationship between  $b_{bp}(590)$  and  $V(D)$ , however the relationship with  $N(D)$  was weak. The strong relationship between  $b_{bp}$  and  $V(D)$  shows that backscattering of particulate matter can be explained by the particulate concentrations as it is a first order influencing factor for variation in the optical properties (Qiu et al., 2016). Figure 23(d) shows that particles with smaller size have high variation in the backscattering coefficient while most of the larger particle sizes all displayed lower backscattering coefficients. The larger particles, from a single sediment sample (S10), were represented by a smaller sample size, thus the spread in the backscattering coefficients may be expected to be less than those of the larger sample (S-OTHER). There may be some value in analyzing the  $b_{bp}(\lambda)$  relationships for individual sediment samples to ascertain the source of the spread in data in Figure 23(a) and (c).

The backscattering spectral slope parameter is relevant in terms of estimating particle sizes. Although the LISST instrument can provide very detailed PSD information, the LISST instrument is known to be sensitive to field deployment, and relative to some multispectral backscattering sensors, is significantly more expensive. A simple three spectral band sensor, such as the EcoTriplet (WetLabs) could potentially provide estimates of relative particle sizes. A comparison between LISST-derived mean particle size and the EcoTriplet-derived gamma parameter measured *in situ* for turbid waters in the Pilbara region showed a very strong relationship (Parnum et al. 2014). The HydroScat-6 and the EcoTriplet essentially operate in the same manner, although the scattering angle for the HydroScat-6S is  $140^\circ$  and for the EcoTriplet is  $124^\circ$ . Nonetheless, the potential for using spectral backscattering angles to determine relative particle sizes can be demonstrated with Hydroscat-6S data and can be applicable to EcoTriplet data.

Figure 24 shows that there is no significant relationship between  $\gamma_{bp}$  and the LISST-derived mean particle size for the sediment samples measured in the tank. However, we see that all the mineral sediment samples (all excluding S10) had  $\gamma_{bp}$  larger than 0.7, except for sample S11 which had  $\gamma_{bp} = 0.38$ . The  $\gamma_{bp}$  is expected to vary between 0 and 2 with higher particles giving smaller  $\gamma_{bp}$  (Antoine et al., 2011). We see a weak trend within Figure 24, but considering the error bars and that almost all sediments were within a mean particle size of 11.2 to 55  $\mu\text{m}$  there is no significant relationship. The fact that sample S10 with a large mean particle size had a small  $\gamma_{bp}$  provides reassurance in the relationship between  $\gamma_{bp}$  and particle size. But in contrast, sample S11 with a mean particle size of 35.9  $\mu\text{m}$  also had a smaller  $\gamma_{bp}$  which could be due to the fact that sample S11 was distinctly different to all other samples, coming from Credo, a terrestrial location inland from Perth, north of Kalgoorlie. The three approaches to deriving  $\gamma_{bp}$ , using data from all 6 backscattering channels, using only three channels, and using just two channels, highlighted the uncertainty in deriving  $\gamma_{bp}$  from scattering data. Only the  $\gamma_{bp}$  values derived using two channels produced values that were considered reasonable. Considering the shape of the spectral backscattering (e.g. Figure 12) if a different reference wavelength had been chosen it is unlikely any of the  $\gamma_{bp}$  values produced would have been reasonable. A reasonable backscattering spectrum is typically expected to display higher scattering at the blue end of the spectrum relative to the red end. The relatively low scattering displayed by the blue channels is likely due to absorption by the red particulates. The fact that the two channels used to derive  $\gamma_{bp}$ , 590 nm and 700 nm, are the two channels at the red end of the spectrum for the Hydroscat-6 may lead to more representative scattering measurements with little effect from particulate absorption. However, the quality of the scattering data may still be influenced by absorption at these wavelengths, as noted above for the weak relationship between  $b_{bp}(\lambda)$  and  $N(D)$  which may be due to particle absorption (Qiu et al., 2016).

We have not demonstrated an effective tank-based capability for estimating basic PSD information from backscattering sensors. We had expected at least a similarly strong relationship as was observed by Parnum et al. (2014), however the reason for the poor results is not clear. We suggest above that it is likely the effect of particle absorption affecting the estimation of the  $\gamma_{bp}$ , but the measurements of Parnum et al. (2014) were in

similar waters affected by dredging. The bimodal PSD may have a more significant effect on the  $\gamma_{bp}$ , and if this is the case we may conclude that the measurements of Parnum et al. (2014) were of more well behaved PSDs.

### 4.3 Particle Densities

The optical determination of particle size (volume) is based on diffraction so does not indicate the amount of porosity or “free space” within the outer extent of a particle. In the case of a floc, for example, the total volume of the floc is determined, where the floc is a combination of mineral particle and water. The density determined by TSM and TVC is therefore termed an “excess density”. If the proportion of water is large relative to particle volume, the excess density is close to that of water, as is typical for flocs. If more particles exist individually rather than as flocs the effective density approaches the particle density. Figure 33 shows the LISST estimated particle excess density (TSS versus TVC slope) – individual sample plots are shown in Appendix E) plotted against the TSS versus NTU slope for the samples collected near Onslow. This demonstrates that both the particle size and density influence the slope of the TSS v NTU relationship.

A suspension of particles representing a large range of sizes may include a range of densities due to a mix of organic particulates (lower densities), flocs (variable densities) or individual mineral type particles (higher densities). With respect to the samples measured in this work we may expect the maximum density of the particles to be relatively high, close to that of the source mineral. Density of carbonates and silicates typically range  $2.0 - 4.5 \times 10^3 \text{ kg m}^{-3}$  (<http://webmineral.com/>) with commonly occurring sedimentary type minerals around  $2.5 \times 10^3 \text{ kg m}^{-3}$ . If we consider fine mineral particles in floc then the excess density could lie in the range  $1.0 - 3.5 \times 10^3 \text{ kg m}^{-3}$  but with commonly occurring sedimentary type mineral flocs around  $1.5 \times 10^3 \text{ kg m}^{-3}$ .

The LISST estimated excess density based on water column samples was  $0.23 \times 10^3 \text{ kg m}^{-3}$  (Fearn et al. 2017b) compared to a range of  $0.96 - 1.61 \times 10^3 \text{ kg m}^{-3}$  for field sediment sample tested in the tank. These results suggest that the tank was measuring more mineral and less clay/biogenic material compared to the field measurements. This may be considered as evidence that flocculation was occurring in the field, where as the freezing, thawing and stirring broke that down for the tank samples.

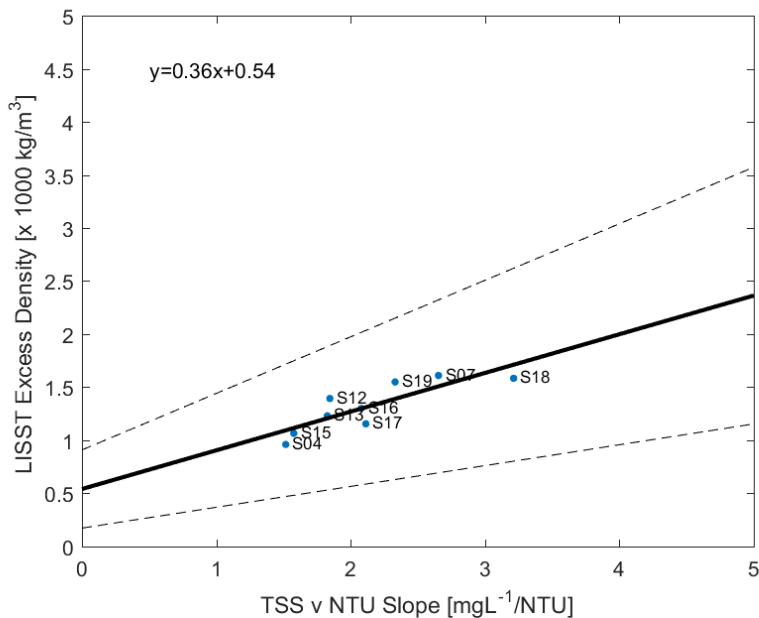


Figure 33. LISST estimated excess density compared to TSS versus NTU slope for Onslow region samples.

## 5 References

- Abdul Wahab, M.A., Fromont, J., Gomez, O., Fisher, R. & Jones, R. (2017) Comparisons of benthic filter feeder communities before and after a large scale-capital dredging program. *Marine Pollution*
- Agrawal, Y.C., Whitmire, A., Mikkelsen, O.A. & Pottsmith, H.C. (2008). Light scattering by random shaped particles and consequences on measuring suspended sediments by laser diffraction. *J. Geophys. Res.*, 113, C04023, doi:10.1029/2007JC004403
- Antoine, D., Siegel, D. A., Kostadinov, T., Maritorena, S., Nelson, N. B., Gentili, B., Velluci, V. & Guillocheau, N. (2011). Variability in optical particle backscattering in contrasting bio-optical oceanic regimes. *Limnology and Oceanography*, 56(3), 955-973. doi:10.4319/lo.2011.56.3.0955
- Bin Omar, A.F. & Bin MatJafri, M.Z. (2009). Turbidimeter Design and Analysis: A Review on Optical Fiber Sensors for the Measurement of Water Turbidity. *Sensors*, 9(10), 8311-8335.
- Dorji, P. & Fearn, P. (2016) A quantitative comparison of total suspended sediment algorithms: A case study of the last decade for MODIS and Landsat-based sensors. *Remote Sensing*, 8, 810; doi:10.3390/rs8100810
- Dorji P, Fearn P, Broomhall M (2016) A Semi-Analytic Model for Estimating Total Suspended Sediment Concentration in Turbid Coastal Waters of Northern Western Australia Using MODIS-Aqua 250 m Data. *Remote Sensing*. 2016; 8(7):556 doi:10.3390/rs8070556 EPA (2016) Technical Guidance: Environmental Impact Assessment of Marine Dredging Proposals. EPA, Western Australia 26 pp.
- Evans, R., Murray, K. L., Field, S., Moore, J. A. Y., Shedrawi, G., Huntley, B. G., . . . Marrable, D. (2012). Digitise This! A Quick and Easy Remote Sensing Method to Monitor the Daily Extent of Dredge Plumes. *PLoS One*, 7(12), 10. doi:10.1371/journal.pone.0051668
- Fearn, P., Broomhall, M. & Dorji, P. (2017a) Optical remote sensing for dredge plume monitoring: a review. Report of Theme 3 - Project 3.1.1, prepared for the Dredging Science Node, Western Australian Marine Science Institution, Perth, Western Australia, 46 pp
- Fearn, P., Dorji, P., Broomhall, M., Chedzey, H., Symonds, G., Shimizu, K., Contardo, S., Mortimer, N., Branson, P. & Sun, C. (2017b). Plume Characterisation. Final Report of Theme 3 Project 3.2.1 of the Western Australian Marine Science Institution (WAMSI) Dredging Science Node. 61 pp.
- Islam, M.A., Smith, A. Lan-Wei, W., Smith, C.J. and Reddy, S., et al. (2007) "Evaluation of satellite remote sensing for operational monitoring of sediment plumes produced by dredging at Hay Point, Queensland, Australia", *J. Appl. Remote Sens.* 1(1), 011506 (December 26, 2007). ;http://dx.doi.org/10.1117/1.2834768
- Lotze, H. K., Lenihan, H. S., Bourque, B. J., Bradbury, R. H., Cooke, R. G., Kay, M. C., . . . Jeremy, B. C. J. (2006). Depletion, Degradation, and Recovery Potential of Estuaries and Coastal Seas. *Science*, 312(5781), 1806-1809.
- Maffione, R. A., & Dana, D. R. (1997). Instruments and methods for measuring the backward-scattering coefficient of ocean waters. *Applied Optics*, 36(24), 6057-6067. doi:10.1364/AO.36.006057
- Mikkelsen, O.A. & Pejrup, M., (2001) . The use of a LISST-100 laser particle sizer for in-situ estimates of floc size, density and settling velocity. *Geo-Marine Letters*, 20:187-195. doi 10.1007/s003670100064
- Mobley, C. D. (1994). *Light and Water: Radiative Transfer in Natural Waters*. San Diego, CA: Academic Press
- Morel, A. (1974). Optical properties of pure water and pure sea water, Chap. In Jerlov & Nielsel (Eds.), *Optical Aspects of Oceanography* (pp. 25-49). New York: Academic Press.
- Morel, A., (1973) Diffusion de la lumiere par les eaux de met. Resultats experimentaux et approach theorique, in *Optics of the Sea*, NATO AGARD Lecture Ser., No. 61, chap. 3.1, 76 pp. Universit6 de Paris, Ville Franche-sur-Mer, France, 1973. (English translation, G. Halikas, 161 pp., Scripps Inst. of Oceanogr., La Jolla, Calif., 1973.)
- Mortimer, N., Symonds, G., Contardo, S., Shimizu, K. & Sun, C. (2015). Plume Characterization - Data report from CSIRO instrumentations during two field trips at Onslow in OCT 2013 and JUN 2014. Theme 2/3.2 Draft Report of the Western Australian Marine Science Institution (WAMSI) Dredging Science Node. 65 pp.
- Mostafa, Y. E. S. (2012). Environmental impacts of dredging and land reclamation at Abu Qir Bay, Egypt. *Ain Shams Engineering Journal*, 3(1), 1-15. doi:http://dx.doi.org/10.1016/j.asej.2011.12.004
- Parnum, I. M., M. Broomhall and P. Fearn (2014). Analysis of data collected by Liquid Robotics' wave gliders around Thevenard Island, northwest Australia: Sortie's 3 and 5, Centre for Marine Science and Technology, Curtin University: Project CMST 1106, Report 2014-14, 11 June 2014 37.
- Qiu, Z., Sun, D., Hu, C., Wang, S., Zheng, L., Huan, Y., & Peng, T. (2016). Variability of Particle Size Distributions in the Bohai Sea and the Yellow Sea. *Remote Sensing*, 8(11), 949.
- Reynolds, R. A., Stramski, D., & Neukermans, G. (2016). Optical backscattering by particles in Arctic seawater and relationships to particle mass concentration, size distribution, and bulk composition. *Limnology and Oceanography*, 61(5), 1869-1890. doi:10.1002/lno.10341
- Reynolds, R. A., Stramski, D., Wright, V. M., & Woźniak, S. B. (2010). Measurements and characterization of particle size distributions in coastal waters. *Journal of Geophysical Research: Oceans*, 115(C8), n/a-n/a. doi:10.1029/2009JC005930
- Sequoia (2011) The influence of particles outside the size range of the LISST. <https://www.sequoiasci.com/article/the-influence-of-particles-outside-the-size-range-of-the-lisst/>
- Sofonia, J.J. & Ensworth, R.K.F (2010) Development of water quality thresholds during dredging for the protection of benthic primary producer habitats. *J. Environ. Monit.* 12. 159-163 Sullivan, J. M., Twardowski, M. S., Zaneveld, J. R. V., Moore, C. M., Barnard, A. H., Donaghay, P. L., & Rhoades, B. (2006). Hyperspectral temperature and salt dependencies of absorption by water and heavy water in the 400-750 nm spectral range. *Applied Optics*, 45(21), 5294-5309. doi:10.1364/AO.45.005294
- Twardowski, M. S., Claustre, H., Freeman, S. A., Stramski, D., & Huot, Y. (2007). Optical backscattering properties of the "clearest" natural waters. *Biogeosciences*, 4(6), 1041-1058. doi:10.5194/bg-4-1041-2007
- Whitlock, C.H., Poole, L.R., Usry, L.W., Houghton W.M., Witte, W.G., Morris, W.D., and Gurganus, E.A., (1981).

"Comparison of reflectance with backscatter and absorption parameters for turbid waters," Appl. Opt. 20, 517-522

Wozniak, S.B. & Stramski, D. (2004) Modeling the optical properties of mineral particles suspended in seawater and their influence on ocean reflectance and chlorophyll estimation from remote sensing algorithms. Applied Optics, 43(17), 3489-3503

Ziegler, A. C. (2003). Issues related to use of turbidity measurements as a surrogate for suspended sediment. Paper presented at the U.S Geological Survey Federal interagency workshop on Turbidity and other sediment surrogates, Reston, VA, United States.

## 6 Appendices

### Appendix A. TSS values for water/sediment samples

ID	Date and Time	TSS Mean	TSS Min	TSS Max	TSS STD
S1	14/09/2015 16:45	1.22	1.22	1.22	0
S1	14/09/2015 16:47	4.02	4.02	4.02	0
S1	14/09/2015 16:50	7.21	7.21	7.21	0
S1	14/09/2015 16:53	11.34	11.34	11.34	0
S1	14/09/2015 16:57	12.57	12.57	12.57	0
S1	14/09/2015 17:02	13.24	13.24	13.24	0
S1	14/09/2015 17:10	17.98	17.98	17.98	0
S1	14/09/2015 17:14	24.69	24.69	24.69	0
S1	14/09/2015 17:18	42	42	42	0
S1	14/09/2015 17:23	88.65	88.65	88.65	0
S2	8/12/2015 10:40	1.5	1.4	1.7	0.14
S2	8/12/2015 10:51	2.9	2.8	3.1	0.14
S2	8/12/2015 10:57	4.57	4.5	4.6	0.05
S2	8/12/2015 11:02	6.27	5.6	6.9	0.53
S2	8/12/2015 11:08	6.63	5	7.6	1.16
S2	8/12/2015 11:44	9.8	9.1	10.3	0.51
S2	8/12/2015 11:50	11.07	10	11.7	0.76
S2	8/12/2015 11:57	11.4	10.1	12.7	1.06
S2	8/12/2015 12:03	13.1	12.1	14.2	0.86
S2	8/12/2015 12:08	17.93	17.3	18.5	0.49
S2	8/12/2015 12:14	22.87	22.2	23.8	0.68
S2	8/12/2015 12:20	26.13	25	27.4	0.98
S2	8/12/2015 12:28	29.47	27.4	30.6	1.46
S2	8/12/2015 12:32	30.8	29.4	31.8	1.02
S2	8/12/2015 12:38	36.87	35.2	37.8	1.18
S2	8/12/2015 12:43	47.13	45	48.6	1.54
S2	8/12/2015 12:50	65.73	62	68.4	2.72
S2	8/12/2015 12:54	91.33	83.2	103.2	8.58
S3	9/12/2015 14:25	1.7	1.5	1.9	0.16
S3	9/12/2015 14:37	1.47	1.4	1.5	0.05
S3	9/12/2015 15:00	1.57	1.5	1.7	0.09
S3	9/12/2015 15:05	1.8	1.5	2.1	0.24
S3	9/12/2015 15:11	1.97	1.8	2.3	0.24

Plume Characterisation – Laboratory Studies

S3	9/12/2015 15:17	2.67	2.4	2.9	0.21
S3	9/12/2015 15:24	2.85	2.39	3.3	0.37
S3	9/12/2015 15:30	3.13	2.29	4.45	0.94
S3	9/12/2015 15:37	37.29	36.26	38.18	0.79
S3	9/12/2015 15:43	20.47	4.74	36.19	15.73
S3	9/12/2015 15:49	4.25	3.93	4.72	0.34
S3	9/12/2015 15:55	5.17	4.94	5.3	0.16
S4	10/12/2015 12:00	1.88	1.55	2.09	0.24
S4	10/12/2015 12:06	2.31	1.96	2.84	0.38
S4	10/12/2015 12:14	3.18	2.81	3.68	0.37
S4	10/12/2015 12:19	4.19	3.86	4.44	0.24
S4	10/12/2015 12:25	4.76	4.25	5.2	0.39
S4	10/12/2015 12:30	4.91	4.39	5.32	0.39
S4	10/12/2015 12:36	5.86	5.31	6.6	0.54
S4	10/12/2015 12:42	6.78	6.61	6.96	0.14
S4	10/12/2015 12:47	40.11	39	41.1	0.86
S4	10/12/2015 12:54	18.9	8.82	37.34	13.06
S4	10/12/2015 13:00	11.4	9.18	12.78	1.59
S4	10/12/2015 13:06	12.97	11.92	13.52	0.74
S5	10/12/2015 15:38	33.83	33.5	34.01	0.23
S5	10/12/2015 15:43	34.01	31.87	35.86	1.64
S5	10/12/2015 15:51	38.01	31.83	41.4	4.38
S5	10/12/2015 15:58	41.7	37.6	45.8	3.35
S5	10/12/2015 16:04	41.9	41	43.3	1
S5	10/12/2015 16:13	42.43	41.8	43.4	0.69
S5	10/12/2015 16:20	42.53	39.1	44.6	2.44
S6	11/12/2015 11:30	2.7	2.2	3	0.36
S6	11/12/2015 11:32	2.2	1.8	2.5	0.29
S6	11/12/2015 11:38	2.17	1.7	2.9	0.52
S6	11/12/2015 11:45	3.17	2.4	4.2	0.76
S6	11/12/2015 11:51	3.23	2.8	4	0.54
S6	11/12/2015 12:21	3.3	2.8	4.1	0.57
S6	11/12/2015 12:27	3.9	3.1	5.2	0.93
S6	11/12/2015 12:33	3.4	3.1	3.6	0.22
S6	11/12/2015 12:41	4.5	3.6	5.1	0.65
S6	11/12/2015 12:58	4.4	3.6	5	0.59
S6	11/12/2015 13:04	5.67	4.5	6.8	0.94
S7	11/12/2015 15:28	2.8	2	3.6	0.8
S7	11/12/2015 15:31	15.83	15.1	16.9	0.77
S7	11/12/2015 15:39	22.7	22	23.6	0.67
S7	11/12/2015 15:45	29.4	28.4	30.6	0.91
S7	11/12/2015 15:51	42.67	39	44.6	2.59
S7	11/12/2015 15:56	109.47	86.6	122.8	16.24
S7	11/12/2015 16:02	113.93	102.8	122.6	8.27
S7	11/12/2015 16:07	73.8	68.8	78.6	4

S7	11/12/2015 16:13	90.13	69.6	102	14.58
S7	11/12/2015 16:19	162.2	103.6	220.8	58.6
S7	11/12/2015 16:26	111.2	108.4	113.2	2.04
S7	11/12/2015 16:33	218.53	188.8	274.8	39.81
S7	11/12/2015 16:39	294.93	248	337.2	36.56
S8	14/12/2015 12:06	2.07	1.7	2.5	0.33
S8	14/12/2015 12:08	5.33	3.5	8	1.93
S8	14/12/2015 12:16	4.47	3.4	6.1	1.17
S8	14/12/2015 12:23	5.37	4.3	6.2	0.79
S9	14/12/2015 14:25	2.67	0.5	5.9	2.33
S9	14/12/2015 14:33	1.97	1.8	2.2	0.17
S9	14/12/2015 14:44	2.47	2.3	2.6	0.12
S9	14/12/2015 14:52	2.27	1.5	3.5	0.88
S10	15/12/2015 11:04	2.1	1.8	2.3	0.22
S10	15/12/2015 11:11	9	8	9.8	0.75
S10	15/12/2015 11:21	13.73	12.7	14.7	0.82
S10	15/12/2015 11:30	20	18.4	21.4	1.23
S10	15/12/2015 11:37	23.8	20.8	27.6	2.83
S10	15/12/2015 11:44	28.33	26	29.6	1.65
S10	15/12/2015 11:51	37.2	34.2	41.6	3.18
S10	15/12/2015 12:00	48.4	46.8	50.8	1.73
S10	15/12/2015 12:09	59.07	55.6	62	2.64
S10	15/12/2015 12:19	59.47	52.4	69.2	7.11
S10	15/12/2015 12:29	70.53	61.6	86	10.98
S11	15/12/2015 14:36	2.17	1.6	2.5	0.4
S11	15/12/2015 14:43	7.67	4.5	9.9	2.3
S11	15/12/2015 14:50	18.1	17.9	18.5	0.28
S11	15/12/2015 14:59	34.37	32	35.6	1.67
S11	15/12/2015 15:05	58	54.2	64.8	4.82
S11	15/12/2015 15:14	64.8	63.6	66	0.98
S11	15/12/2015 15:21	85.47	82.2	87.6	2.35
S11	15/12/2015 15:30	141.07	100.4	206.8	46.91
S11	15/12/2015 15:37	137.33	132.4	143.6	4.67
S11	15/12/2015 15:45	135.87	129.6	143.6	5.81
S11	15/12/2015 15:54	138.13	119.2	149.6	13.49
S11	15/12/2015 16:04	183.2	172.4	197.2	10.37
S12	16/12/2015 10:52	3.33	2.5	4.4	0.79
S12	16/12/2015 10:57	10.9	8.3	13.5	2.12
S12	16/12/2015 11:06	13.43	12.3	14.4	0.87
S12	16/12/2015 11:14	20.37	18.5	21.6	1.34
S12	16/12/2015 11:23	32.67	28.6	35.2	2.9
S12	16/12/2015 11:30	35.4	34.2	37.6	1.56
S12	16/12/2015 11:36	37	35.4	38.4	1.23
S12	16/12/2015 11:46	46	44.8	48	1.42
S12	16/12/2015 11:51	58.8	47.6	70.4	9.31

S12	16/12/2015 12:00	60.4	57.6	62.4	2.04
S12	16/12/2015 12:08	68	66.4	69.6	1.31
S13	16/12/2015 14:24	2.6	2	3.2	0.49
S13	16/12/2015 14:32	8.67	7.8	10.2	1.09
S13	16/12/2015 14:39	19.67	18	20.8	1.2
S13	16/12/2015 14:48	32.1	26.9	35.2	3.7
S13	16/12/2015 14:54	57.27	50.6	61.2	4.74
S13	16/12/2015 15:01	71.13	61.4	85.4	10.31
S13	16/12/2015 15:08	84.47	81.4	86.4	2.19
S13	16/12/2015 15:15	101.73	92.8	110	7.04
S13	16/12/2015 15:21	122	117.6	127.6	4.17
S13	16/12/2015 15:33	121.6	99.6	135.2	15.7
S13	16/12/2015 15:39	160.67	144	179.2	14.43
S14	8/11/2016 12:46	2.57	1.8	3.6	0.76
S14	8/11/2016 12:48	19.13	11	35.2	11.36
S14	8/11/2016 12:53	36	22.6	42.9	9.48
S14	8/11/2016 13:02	37.27	31.2	43.5	5.02
S14	8/11/2016 13:11	35.2	31.8	41.4	4.39
S14	8/11/2016 13:16	44.67	39	49	4.19
S14	8/11/2016 13:24	51.4	40.2	60.2	8.34
S14	8/11/2016 13:31	51.47	45.6	62.4	7.74
S14	8/11/2016 13:37	65.07	59.2	74.4	6.67
S14	8/11/2016 13:45	76.93	72.8	79.6	2.96
S14	8/11/2016 13:52	96.4	96	96.8	0.33
S14	8/11/2016 14:23	151.87	140.4	160.8	8.52
S14	8/11/2016 14:44	220.6	190.4	237.4	21.4
S15	9/11/2016 8:40	3.63	3.3	4.1	0.34
S15	9/11/2016 8:41	11.6	8.8	14.3	2.25
S15	9/11/2016 8:59	22.97	21.3	25.2	1.64
S15	9/11/2016 9:05	33.3	30.4	38.2	3.48
S15	9/11/2016 9:14	48.4	41.2	55.4	5.8
S15	9/11/2016 9:21	61.8	52	70	7.44
S15	9/11/2016 9:30	74.6	67	88.6	9.91
S15	9/11/2016 9:37	109.27	96	120.4	10.07
S15	9/11/2016 9:44	95.8	88.4	103.2	7.4
S16	9/11/2016 11:32	2.93	1.8	4.2	0.98
S16	9/11/2016 11:40	9.93	8.8	10.8	0.84
S16	9/11/2016 11:49	17.17	15.2	18.8	1.49
S16	9/11/2016 11:55	33.2	31	35.2	1.72
S16	9/11/2016 12:03	46.13	37.4	61.8	11.1
S16	9/11/2016 12:13	50.93	46.4	58.2	5.19
S16	9/11/2016 12:19	62	54	73.2	8.16
S16	9/11/2016 12:25	86.13	72	100	11.43
S17	9/11/2016 14:38	3.83	2.8	4.8	0.82
S17	9/11/2016 14:40	34.73	29.9	41.9	5.17

Plume Characterisation – Laboratory Studies

<b>S17</b>	9/11/2016 14:48	50.63	48.1	53.5	2.22
<b>S17</b>	9/11/2016 14:54	61.97	50.6	71.8	8.72
<b>S17</b>	9/11/2016 15:00	85.2	77	90	5.83
<b>S17</b>	9/11/2016 15:06	87.27	75.2	94	8.55
<b>S17</b>	9/11/2016 15:14	125.73	116.8	140	10.19
<b>S17</b>	9/11/2016 15:20	152.27	127.6	173.2	18.8
<b>S17</b>	9/11/2016 15:26	148.67	141.2	155.6	5.89
<b>S18</b>	10/11/2016 11:02	9.87	9.2	11	0.81
<b>S18</b>	10/11/2016 11:10	32	26.2	38.9	5.24
<b>S18</b>	10/11/2016 11:17	97.27	71.6	132.4	25.71
<b>S18</b>	10/11/2016 11:27	155.8	124	198	31.09
<b>S18</b>	10/11/2016 11:36	142.93	121.6	172.6	21.64
<b>S18</b>	10/11/2016 11:47	260.8	221.6	296	30.51
<b>S18</b>	10/11/2016 11:53	404.13	311.2	456.4	65.88
<b>S18</b>	10/11/2016 12:00	483.47	423.2	574.4	65.43
<b>S19</b>	10/11/2016 13:50	3.57	2.8	4.1	0.56
<b>S19</b>	10/11/2016 13:59	41.95	41.6	42.3	0.35
<b>S19</b>	10/11/2016 14:11	35.87	32.8	39.8	2.92
<b>S19</b>	10/11/2016 14:18	73.93	61.8	82.4	8.8
<b>S19</b>	10/11/2016 14:24	104.4	93.4	125.8	15.13
<b>S19</b>	10/11/2016 14:28	118	106.4	131.6	10.38

Appendix B. NTU time series.

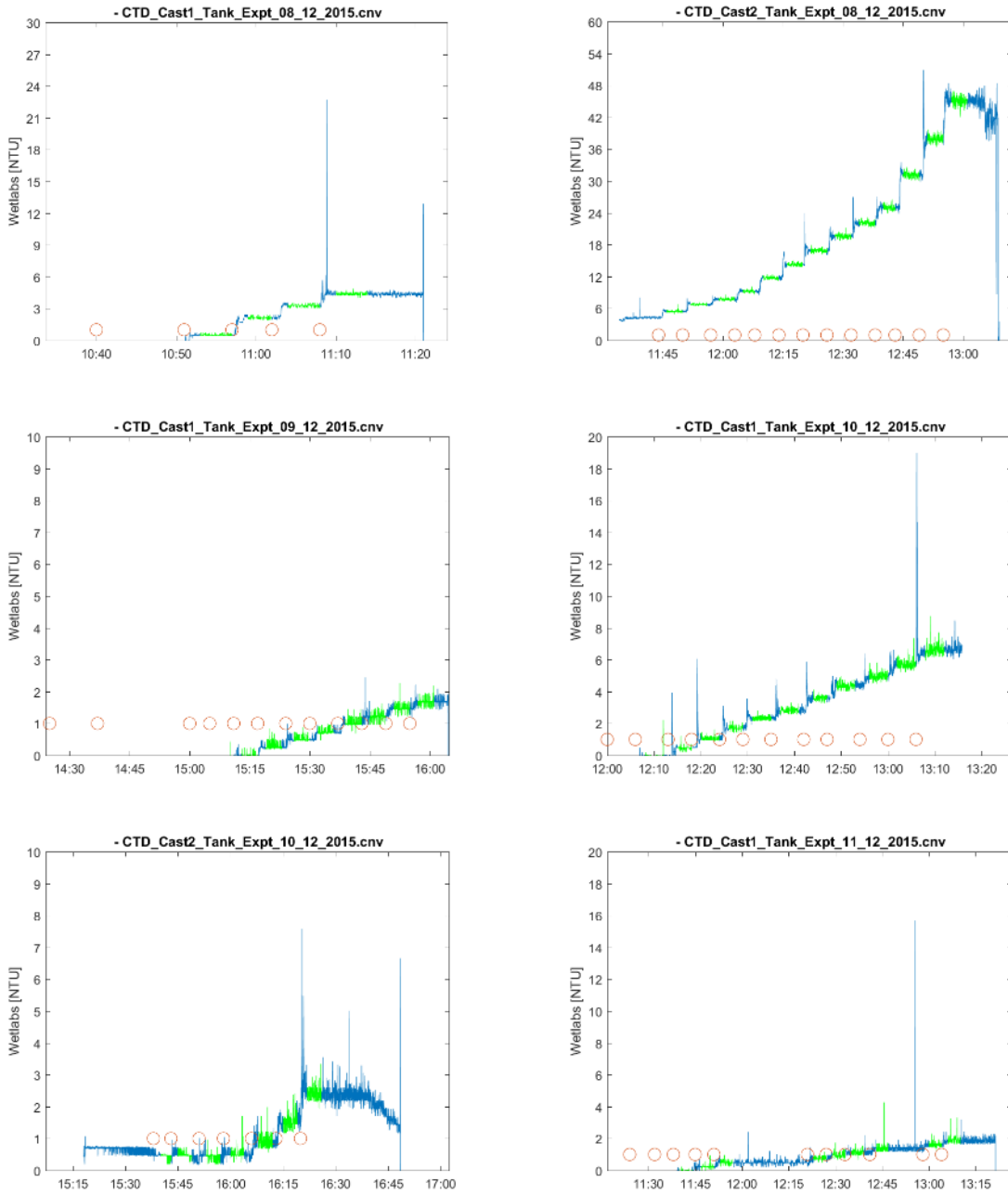


Figure 34. NTU time series. Samples 1-6.

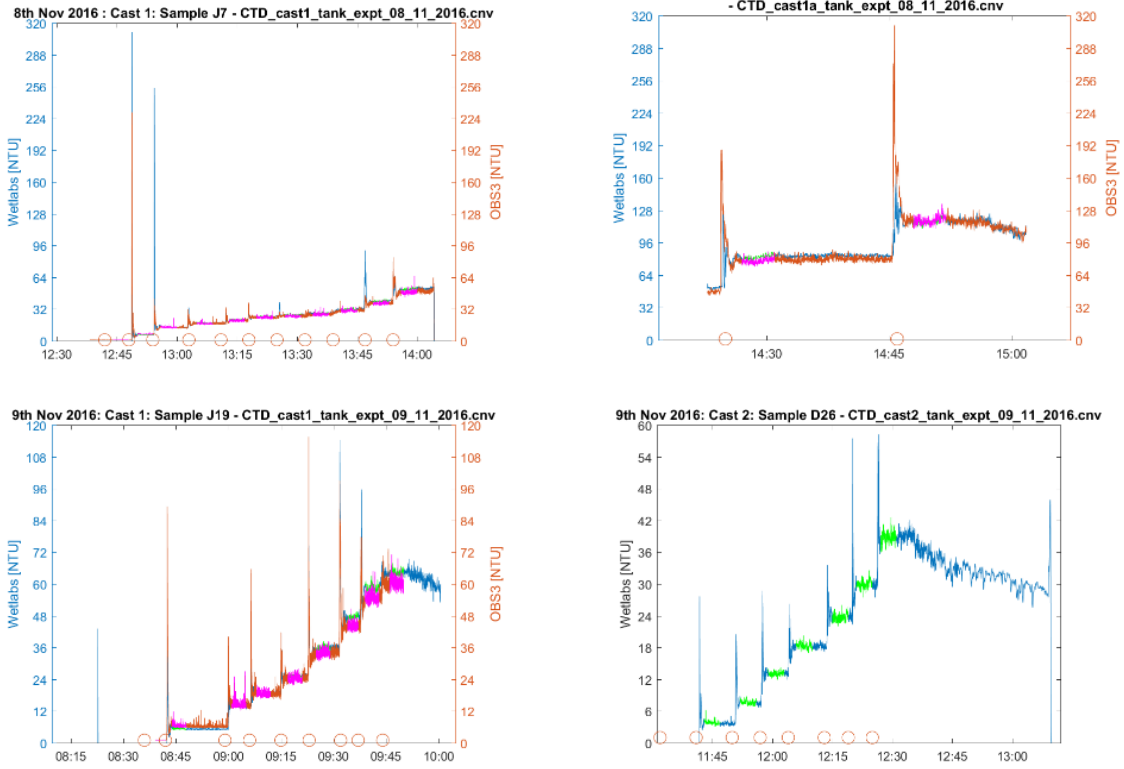


Figure 35. NTU time series. Samples 13-16.

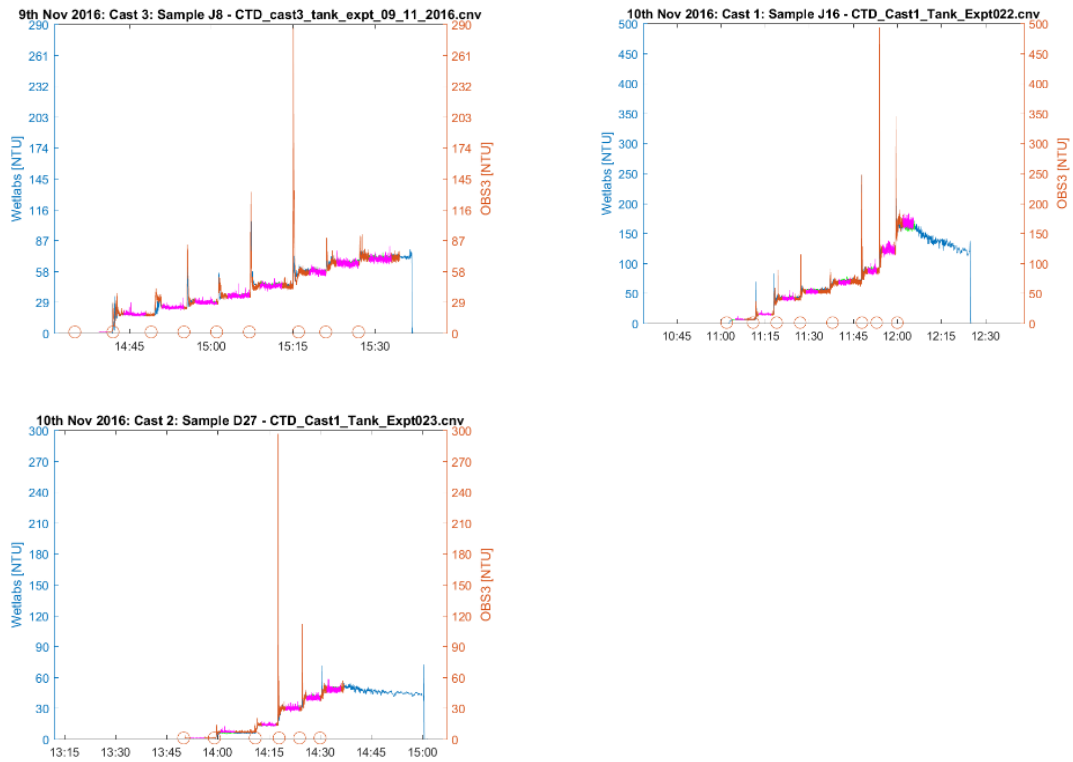


Figure 36. NTU time series. Samples 17-19.

Appendix C. TSS vs OBS NTU regressions.

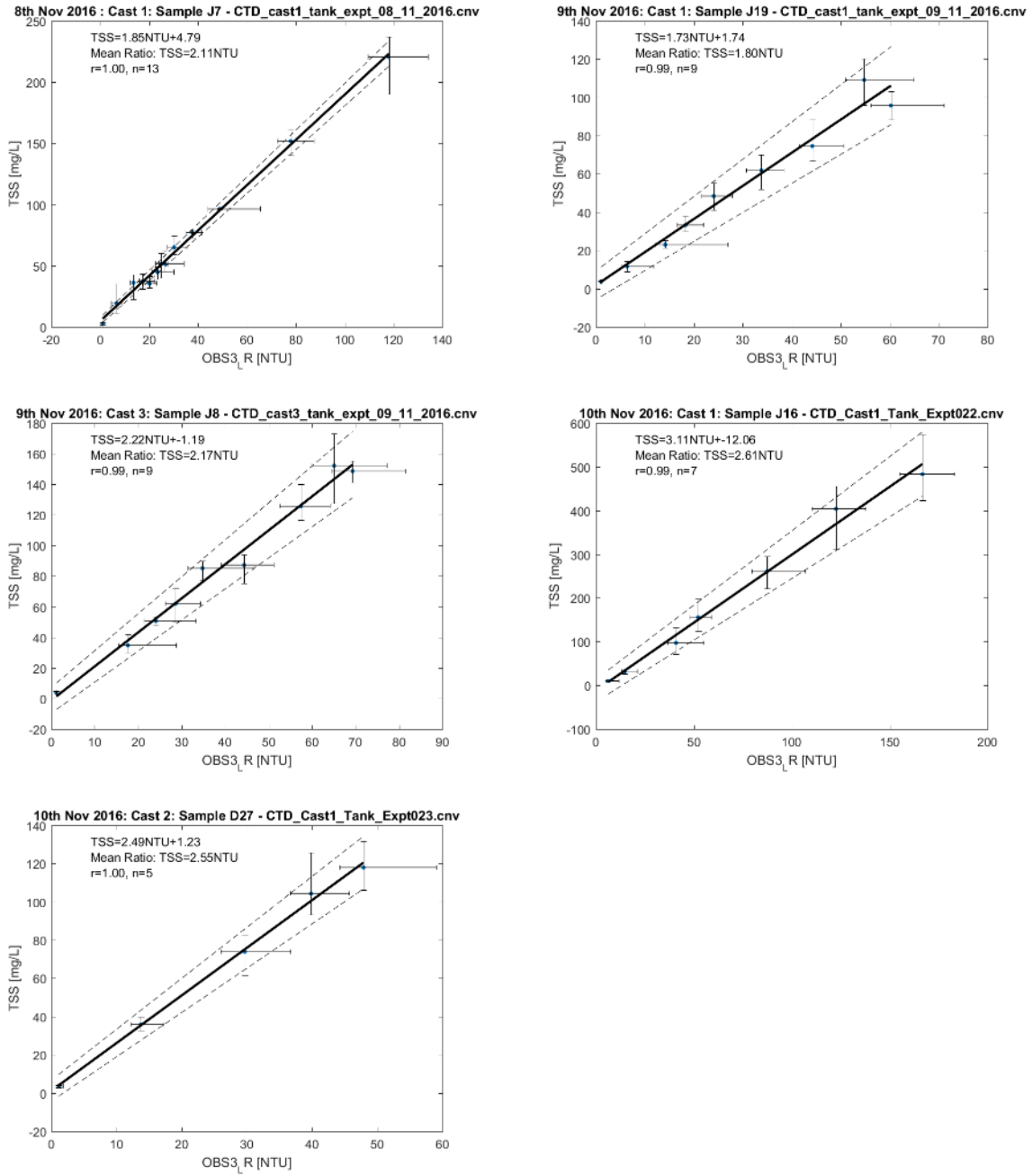


Figure 37. TSS vs OBS3 regressions for low-range OBS setting. Samples 13, 15, 17, 18 and 19.

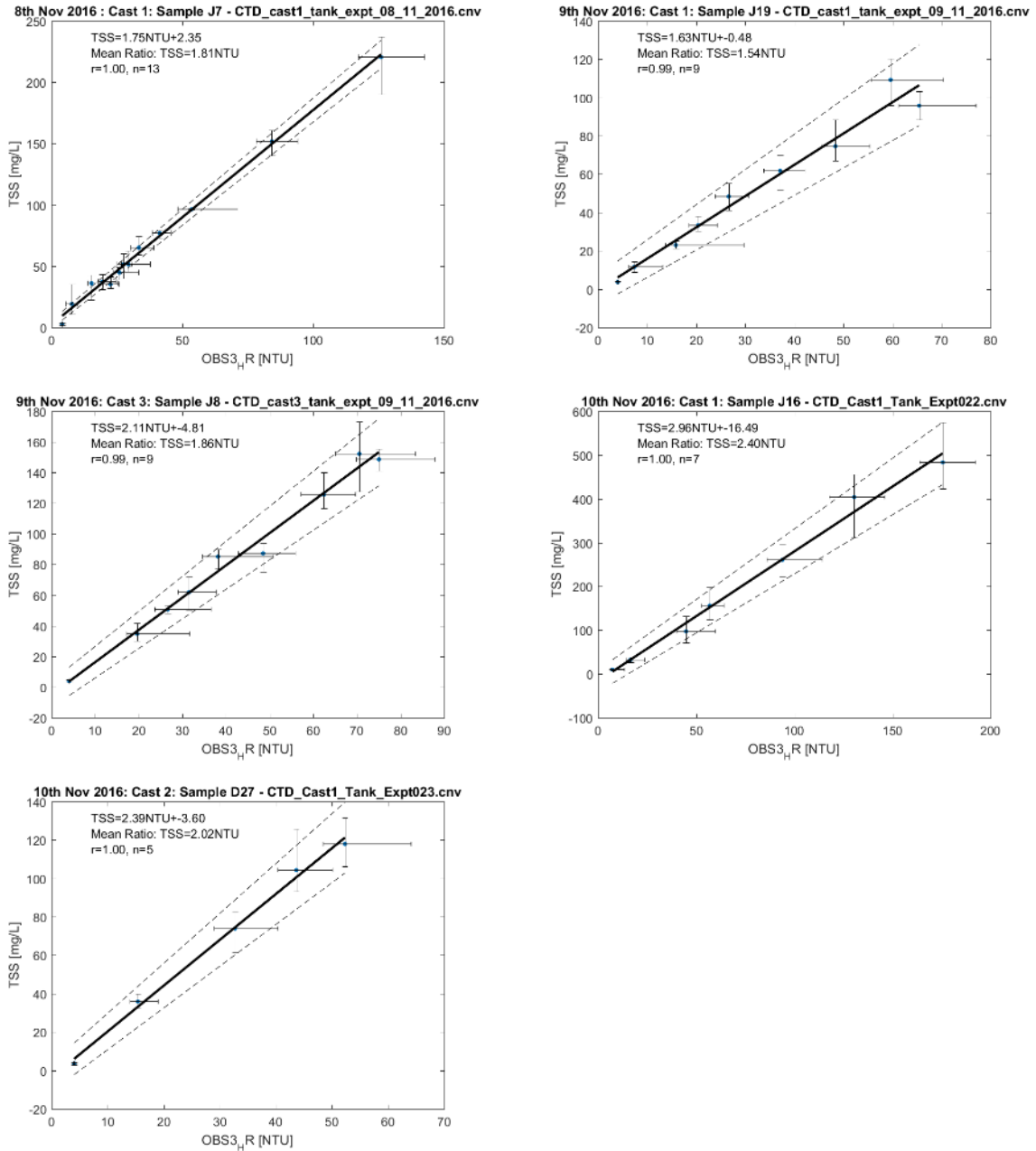


Figure 38. TSS vs OBS3 regressions for high-range OBS setting. Samples 13, 15, 17, 18 and 19.

Appendix D. TSS vs Wetlabs NTU regressions

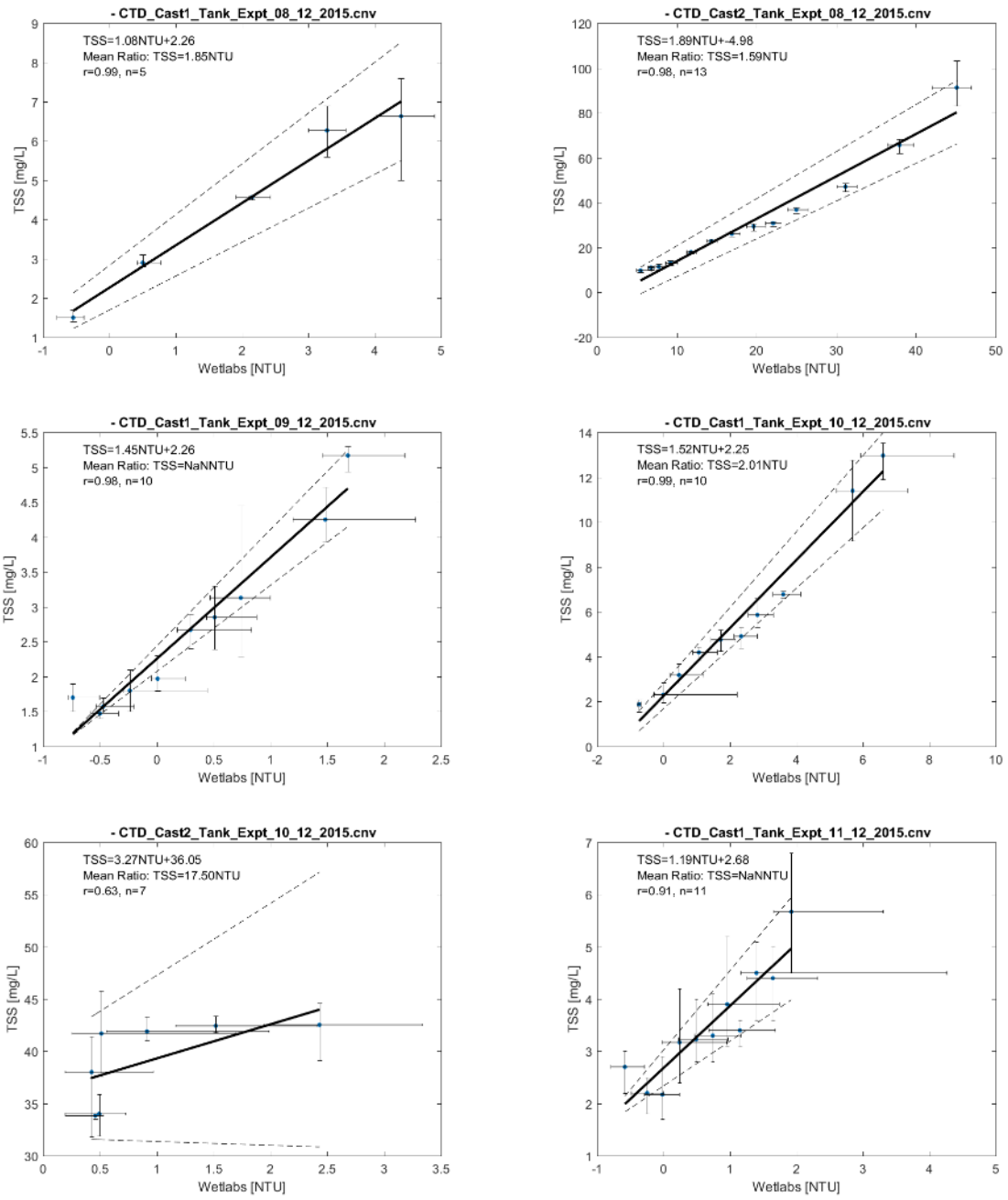


Figure 39. TSS vs NTU regressions. Samples 1-6.

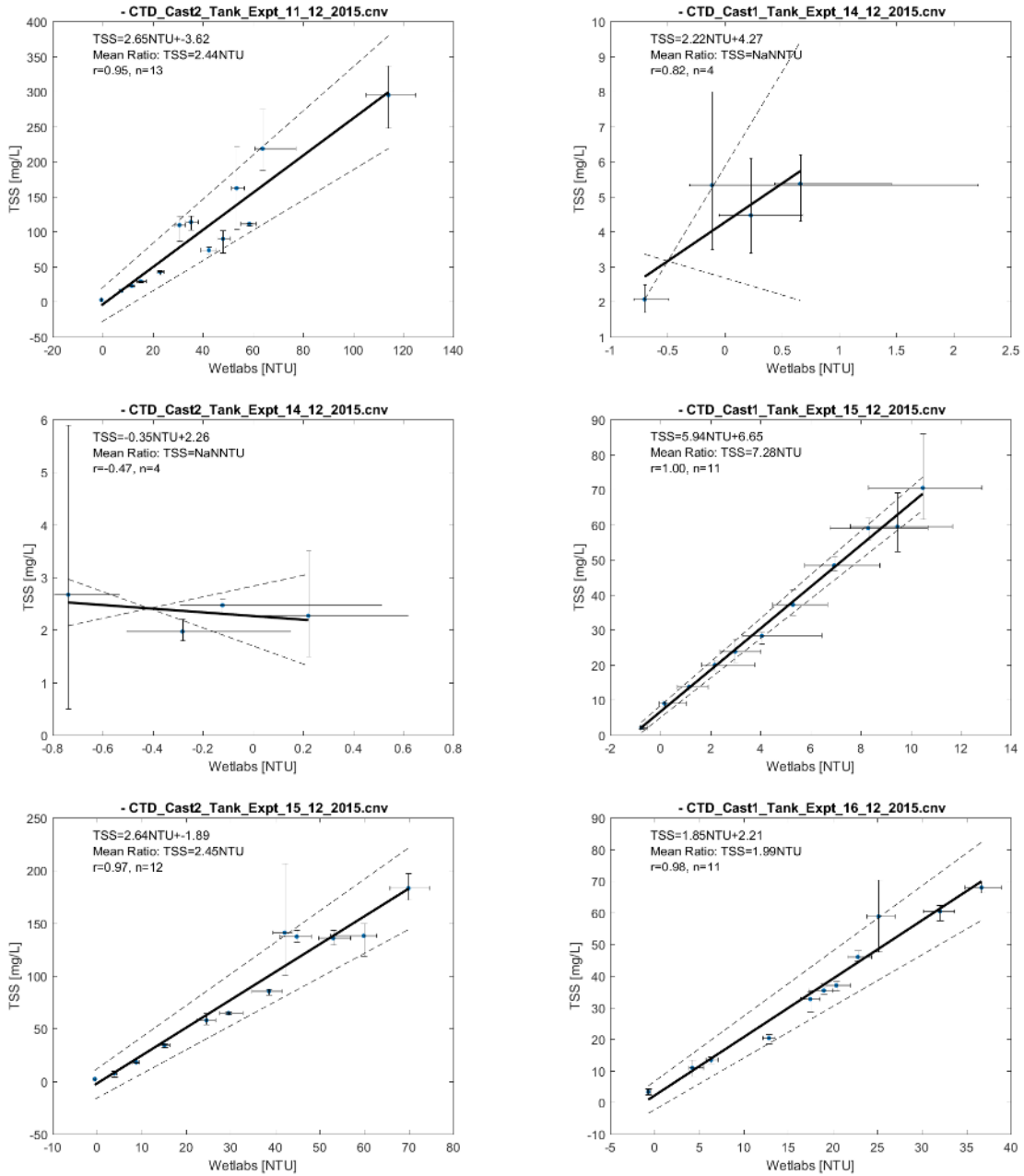
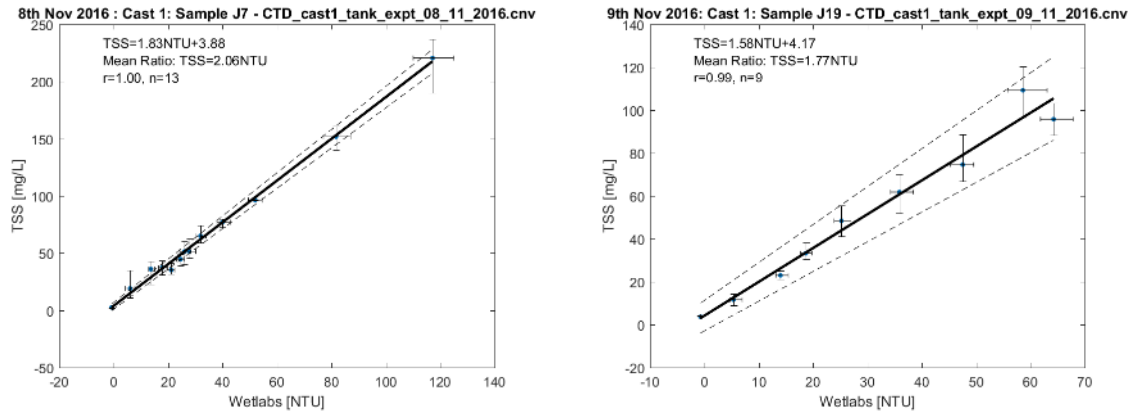


Figure 40. TSS vs NTU regressions. Samples 7-12.



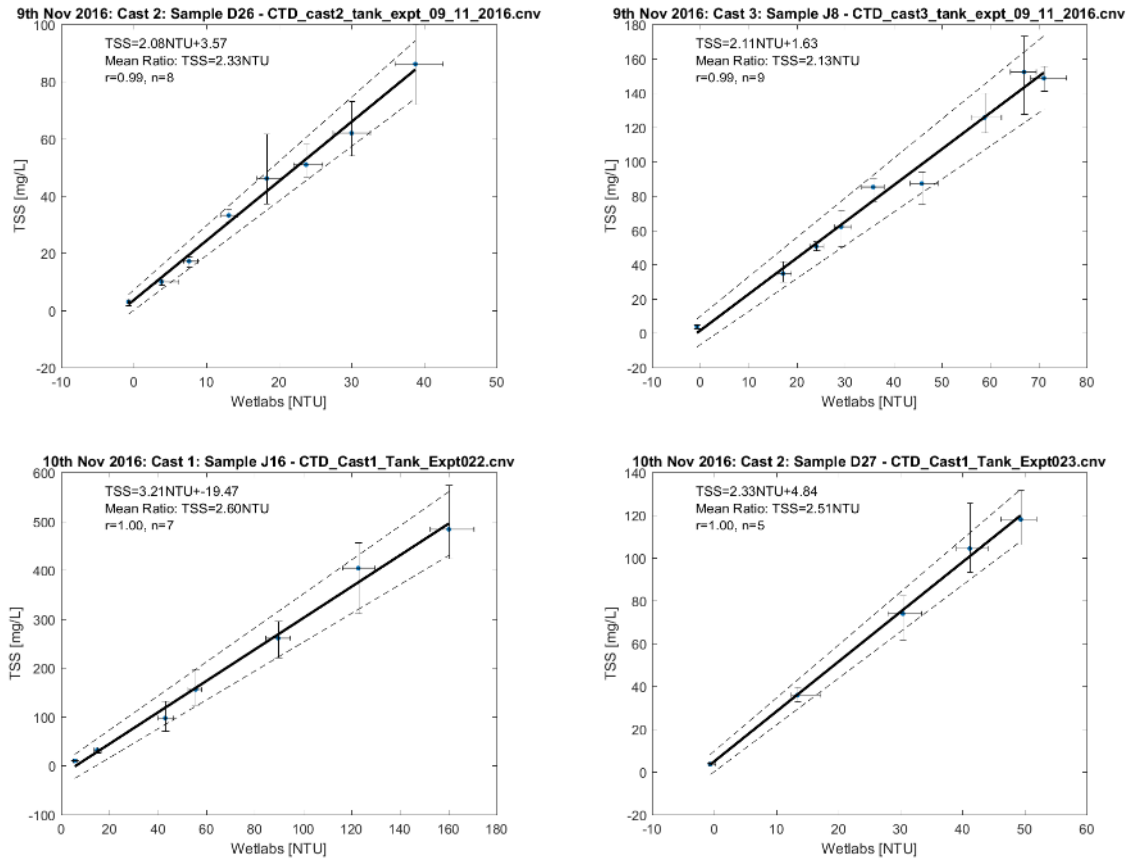


Figure 41 TSS vs NTU regressions. Samples 13, 15-19.

Appendix E. TSS vs LISST total volume concentration regressions.

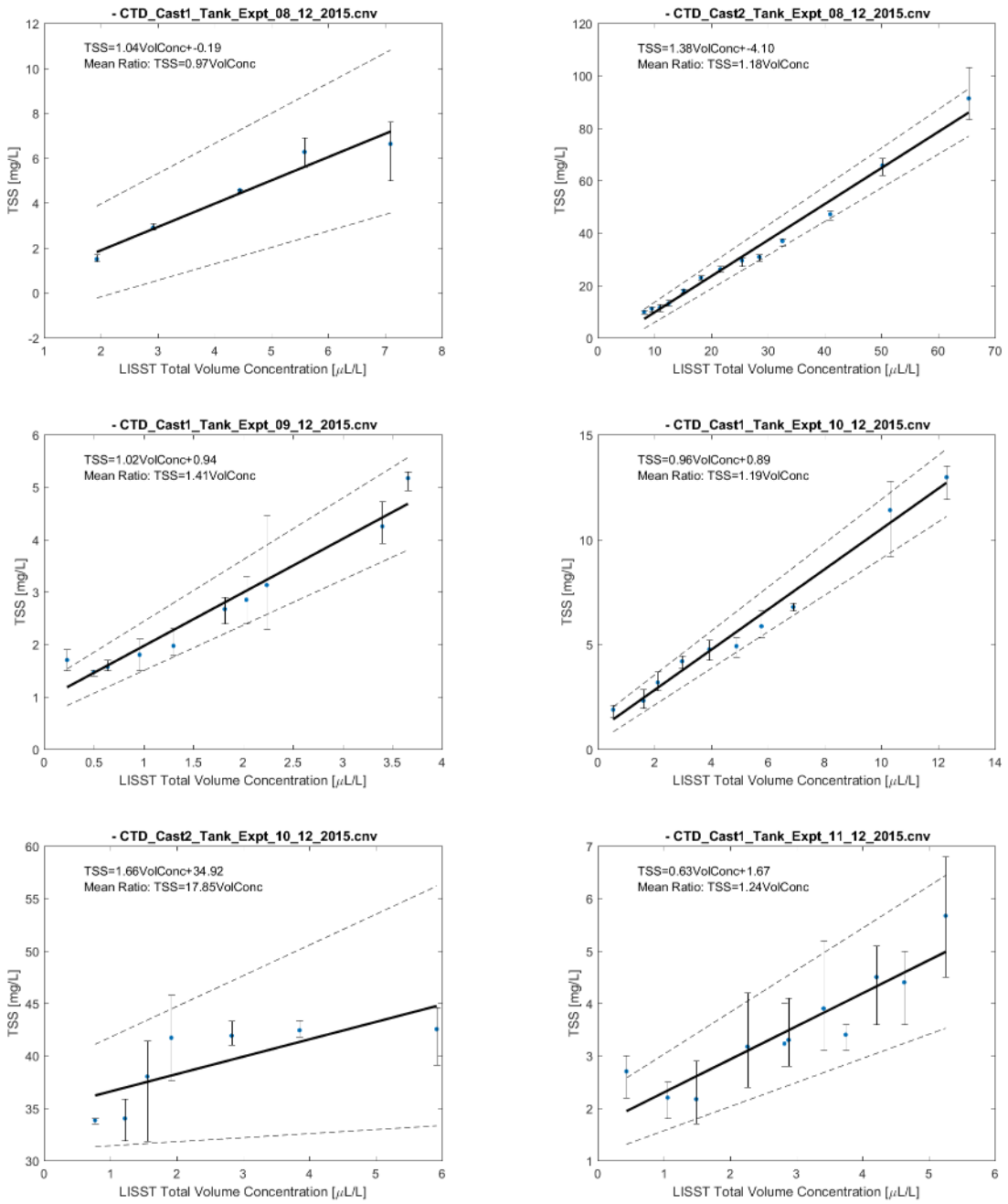
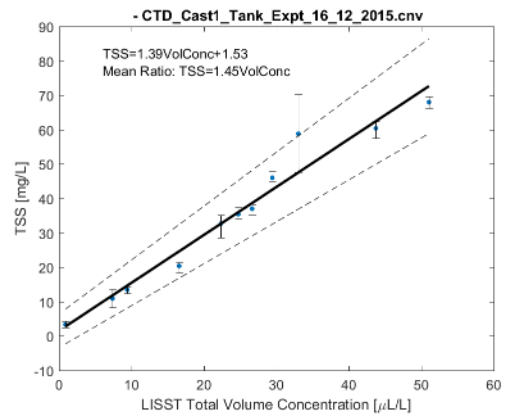
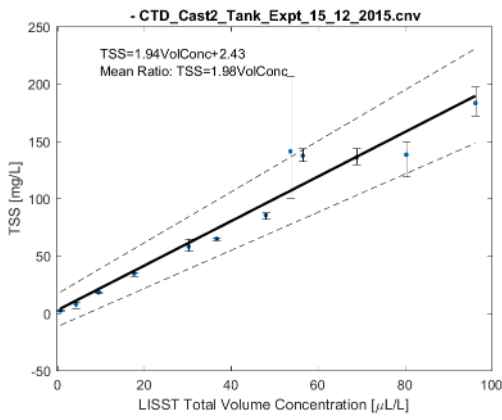
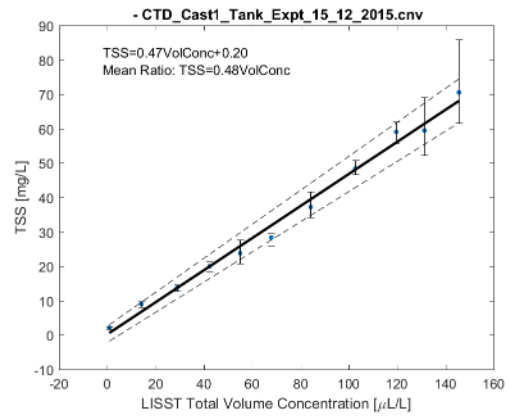
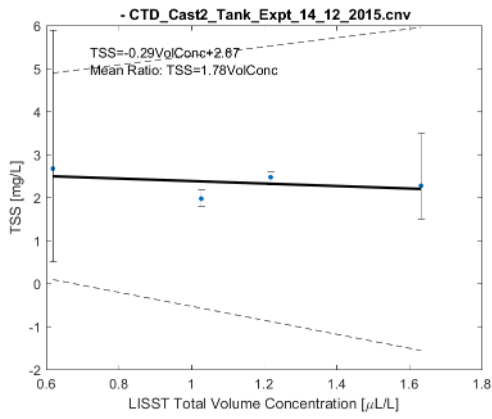
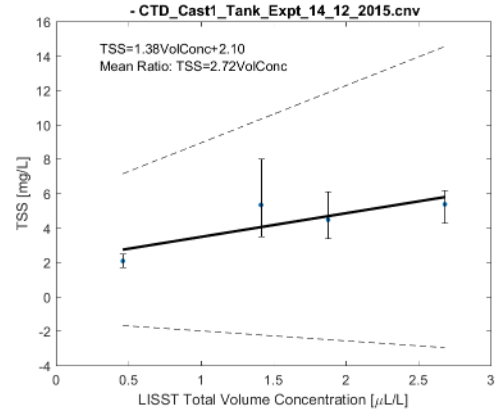
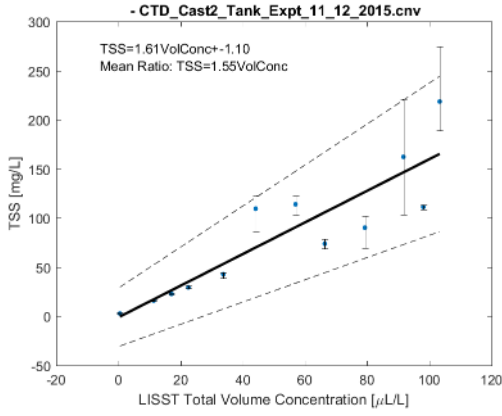


Figure 42. TSS versus Total Volume Concentration. Samples 1-6.



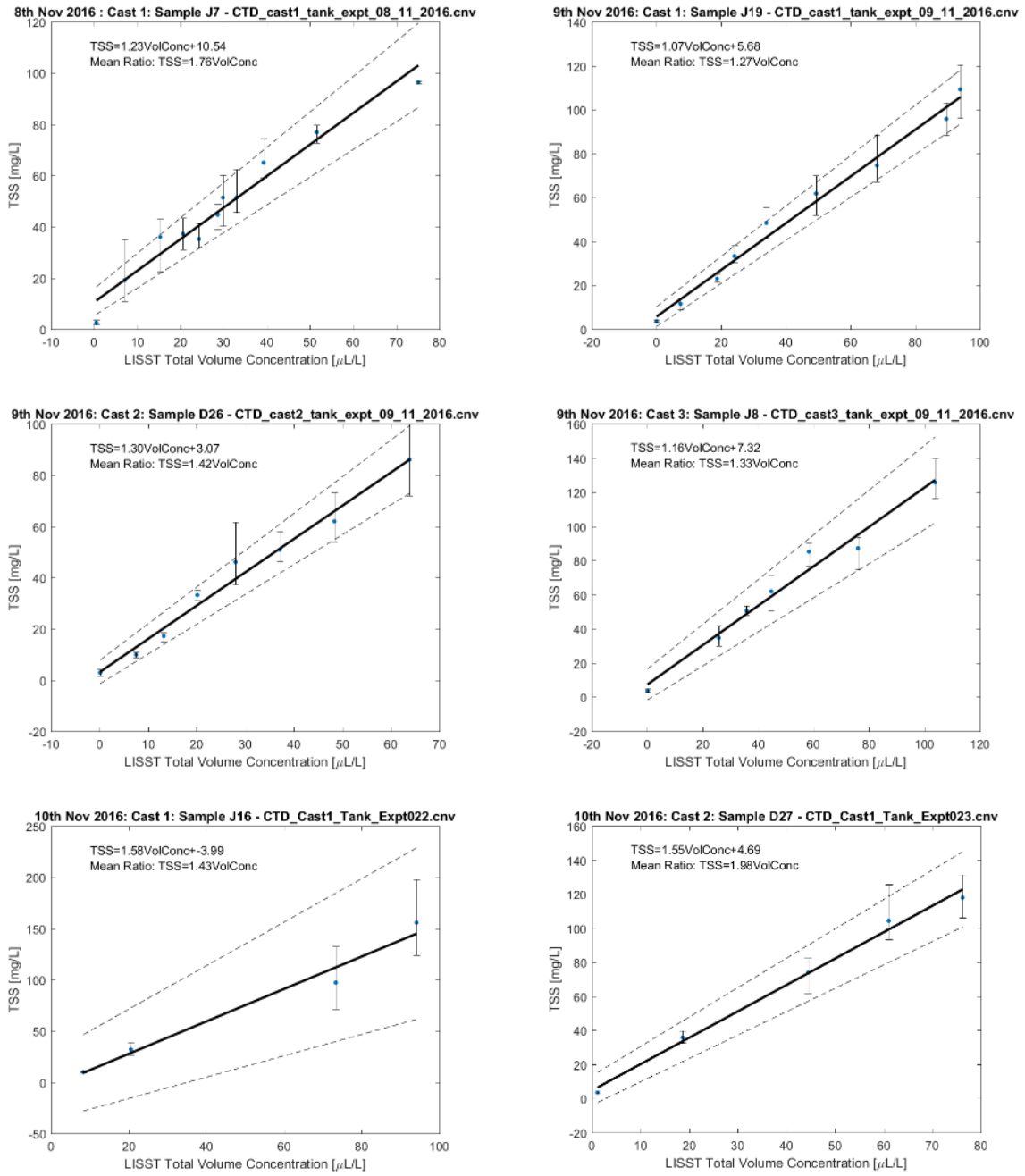


Figure 43. TSS versus Total Volume Concentration. Samples 13, 15-19.